

High Precision Positioning and Low Velocity Control of a Permanent Magnet Synchronous Motor



Hampus Isaksson
Patrik Önnheim

Division of Industrial Electrical Engineering and Automation
Faculty of Engineering, Lund University

High Precision Positioning and Very Low Velocity Control of a Permanent Magnet Synchronous Motor

Hampus Isaksson & Patrik Önnheim



LUND
UNIVERSITY

Department of Automatic Control &
Division of Industrial Electrical Engineering and Automation

M.Sc. Thesis

ISRN LUTFD2/TFRT-5963-SE

ISSN 0280-5316

or CODEN:LUTEDX/(TEIE-5351)/1-89(2015)

Printed in two editions for:

Department of Automatic Control and

Division of Industrial Electrical Engineering and Automation (IEA)

Lund University

Box 118 SE-221 00 LUND

Sweden

© 2015 by Hampus Isaksson & Patrik Önnheim. All rights reserved.

Printed in Sweden by Media-Tryck.

Lund 2015

Abstract

The purpose of this report is to evaluate a direct driven permanent magnet motor in high accuracy position and low speed operation. Actuation in this case is usually accomplished by stepping motors combined with belts and pulleys. High accuracy positioning is considered to be within 0.1 degrees and low speed 0.05 degrees per second, while at the same time have a 180 degree step response within 0.5 second.

A model is derived of the motor along with methods for model parameter identification. This model is the basis for simulation of the motor in closed loop control. A prototype is developed in order to prove the validity of the results made by simulations. Experiments on the prototype resulted in two control methods, namely field oriented control and synchronous control.

Conclusions drawn from the projects are as follows. The simulations do mirror the inherent problems with the permanent magnet motor. The prototype developed for the project is functioning and highly capable. Field oriented control was unable to meet the specified requirements. However, combined with iterative learning control the performance was improved significantly. Synchronous control satisfied most of the requirements, although its responsiveness and low efficiency are possible areas of improvement in future research.

Acknowledgements

We would like to thank Anders Sandahl, Martin Furmanski, Zakaria Maghder and their colleagues at Axis Communications AB; as well as Anders Robertsson and Gunnar Lindstedt at Lund University for good guidance and support throughout this project.

Contents

Abstract	iii
Acknowledgements	iv
Contents	v
1 Introduction	1
1.1 Disposition	1
1.2 Division of Labor	2
2 Background	3
2.1 Project Stakeholder	3
2.2 Goals	3
2.3 Problem Formulation	4
2.4 Scope	4
3 Methodology	7
4 Permanent Magnet Motors	9
4.1 Construction	9
4.2 Back Electromotive Force	11
4.3 Electromagnetic Torque	12
4.4 Cost	12
4.5 Summary	13
5 Prototype	15
5.1 Introduction	15
5.2 Control Unit	17
5.3 Software	17
5.3.1 FPGA	17
5.3.2 RT	17
5.3.3 Closed Loop Control	18
5.3.4 Implementation on Other Hardware	19
5.4 Voltage Source Inverter	19
5.5 Position Sensor	20

5.6	Measuring Velocity	21
5.7	Current Sensor	21
5.7.1	Analog Current Filter	22
5.8	Motor	23
5.8.1	Necessary Torque Estimation	23
5.8.2	Power Consumption Restraint	24
6	Dynamic Modeling	27
6.1	Friction	27
6.1.1	Friction Model	27
6.2	Reference Frame Transformation	29
6.3	System Equations	30
7	Parameter Identification	33
7.1	Phase Resistance	33
7.2	Direct and Quadrature Inductance	34
7.3	Back-emf & Torque Constant	36
7.4	Cogging Torque	37
7.5	Friction Parameter Identification	37
8	Space Vector Modulation	39
8.1	Principle of Operation	39
8.2	Switching Sequence	43
9	Field-Oriented Control	45
9.1	Theory	45
9.2	Simulation	47
9.3	Results	50
9.3.1	Step Response Angle	50
9.3.2	Constant Low Angular Velocity	52
9.3.3	Step Response Angular Velocity	52
10	Synchronous Control	55
10.1	Theory	55
10.2	Results	57
10.2.1	Step Response Angle	57
10.2.2	Constant Low Angular Velocity	59
10.2.3	Step Response Angular Velocity	59
11	Compensation Methods	61
11.1	Estimation of Speed	61
11.2	Friction	62
11.3	Cogging Torque	63
11.3.1	Iterative Learning Control	63
11.3.2	Simulated Counter Torque	63
11.3.3	Angular Position Mapping	64
11.3.4	Sinusoidal Counter Torque	65
11.4	Results	66

11.4.1 Iterative Learning Control	66
11.4.2 Simulated and Sinusoidal Counter Torque	69
12 Discussion	71
13 Conclusion	73
13.1 Future Work	74
 Bibliography	 75

*Dedicated to our families and friends for their support throughout
our education.*

Chapter 1

Introduction

1.1 Disposition

Chapter 1 describing the background with a disclosure of the project stakeholder company followed by main goals, questions that will be investigated and the scope of the project.

Chapter 2 gives an account of and motivation for the methodology used for the project.

Chapter 4 introduces the two types of permanent magnet motors, how they are constructed and what differentiates them. This knowledge will be the basis for a recommended motor design for the project.

Chapter 5 describes the prototype that has been developed for the project. It also accounts for design considerations for each part of the prototype, such as necessary torque output calculation and how to measure current.

In Chapter 6 a mathematical model of the motor is derived. Assumptions that are made in the process of developing this model will be accounted for. The systems equations in this chapter form the basis for simulations further on.

Parameters in the motor model are either experimentally identified or validated in Chapter 7.

The method of generating sinusoidal phase currents with space vector modulation is described in Chapter 8.

Chapter 9 presents field-oriented control which is one of two control laws that are evaluated in the project. Simulation of the closed loop system performance is presented

followed by actual tests on the prototype. In a similar fashion Chapter 10 describes the synchronous control which is the second method that is evaluated in the project.

Methods for compensating some of the inherent problems with the control application are described in chapter 11. The most appropriate of these methods will be tested on the prototype.

Chapter 12 evaluates results made from each of the control methods and conclusions along with future research recommendations are given in Chapter 13.

1.2 Division of Labor

The authors of this thesis has taken equal part in all of the work that is related to the project.

Chapter 2

Background

2.1 Project Stakeholder

Axis Communications AB is an IT company offering network video solutions for professional installations. Their products and solutions focus on security surveillance and remote monitoring [1]. As of the third quarter of 2014 the company has over 1800 employees with offices in more than 40 countries [2].

A portion of the cameras on offer use electric motors for remote positioning, called pan-tilt-zoom (PTZ) cameras. Actuation in these cameras is usually accomplished using stepping motors, pulleys and belts for the pan/tilt-system. This solution is often quite expensive and complex, therefore an alternate solution would be preferable.

It is possible to use a direct drive permanent magnet motor (PMM) combined with a position sensor in order to get a cost effective and reliable solution. However when comparing performance there is room for improvement of the direct drive system. This project was started in order to investigate possible improvements from a control system's perspective. This could be done by counteracting the inherent weaknesses of the PMM; for example minimizing power consumption during steady state, removing overshoot in step responses or increase its ability to withstand vibrations.

2.2 Goals

The first objective of this project is to derive a mathematical model of the PMM and then investigate how to identify the model parameters. The second objective is to determine a suitable control method and then develop a direct drive prototype using this method.

2.3 Problem Formulation

This report will investigate and give answers to the following three problems. A solution to each of these problems are considered critical to reach the project goals.

1. Ways to overcome static friction and cogging torque when micro-positioning the system.
2. Evaluate whether or not the control algorithm is portable to a micro-controller. Try to simulate the limited performance of a given micro-controller.
3. The ability to handle changes in reference or load disturbances while having a boundary condition on power consumption.

The importance of the first question cannot be emphasized enough. The PTZ-camera should be able to follow objects at long distances. This translates to high accuracy in positioning the camera as well as having smooth rotation at extraordinary low angular velocity.

The second and third questions deal with the feasibility of turning the prototype into a product that can cost-effectively be mass produced.

A working prototype had to be built from scratch in order to answer these questions. For this reason a number of more trivial problems will be investigated, such as:

- What size and type of motor is suitable for the given application;
- What type of motor driver circuit should be used and how to dimension it in order to match the size of the motor;
- What type of sensors are needed and how to implement them.

2.4 Scope

A specification of requirements have been set in agreement with the stakeholder company as a reference for evaluating the performance of the prototype, see Table 2.1. The focus of this report is on the development of a prototype that in some aspect is a performance improvement relative to these requirements.

Two levels of system requirements have been identified. Medium expectations corresponds to current performance of a PMM in the given application whereas the high expectations represent the performance of a stepper motor in the same application.

TABLE 2.1: System requirements

Description	Expectations		Priority
	Medium	High	
Min. angular velocity [$^{\circ}s^{-1}$]	0.20	0.05	Critical
Time needed for half rotation [s]	0.5	0.5	Normal
Steady state position error without load [$^{\circ}$]	≤ 0.35	≤ 0.1	Critical
Steady state position error with load [$^{\circ}$]	≤ 0.35	≤ 0.1	Normal
Max. power consumption [W]	5	NA	Critical
Continuous power consumption [W]	3	NA	Normal

Minimum angular velocity is of special interest for the given application since the camera needs to track objects at a long distance. Of special note for this application is that there should be extremely low ripple in angular velocity. No demand for torque output has been determined, instead time needed for a half rotation position step has been identified.

Chapter 3

Methodology

Research and work that led to the final prototype was done according to the action research methodology, see Figure 3.1. The justification for choosing this method is that it is common for problem solving projects [3].

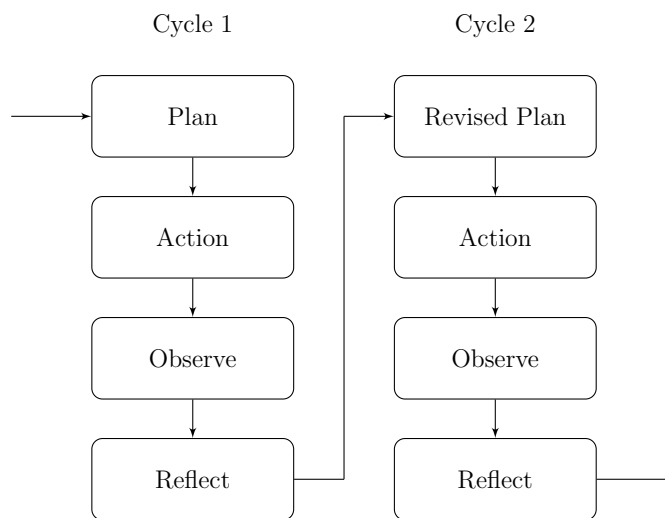


FIGURE 3.1: Workflow according to the action research model.

Each step along the way from project start-up to final prototype can by itself be divided into several cycles in the model. A great example of this is when measuring direct and quadrature inductance described in Section 7.2. Measurements were planned and carried out according to literature. However, when observing the results they contradicted theory, as such the measurement methodology was iteratively refined until measurement data made sense.

Proper scientific methodology requires that results of experiments can be reproduced. Therefore each measurement made will be elaborated upon and the prototype will be described in detail.

When several approaches are available for solving a specific type of problem, a critical evaluation will be made in order to defend the chosen method. By doing so the reader will become aware of the rationale behind every decision made.

Control parameters and motor measurements that are presented in this report is naturally related to the type of motor and load. The validity of these results for another motor of the same type is directly related to motor production variation and prototype sensor accuracy and precision. Regarding generalization of the solution to other PMMs, the authors are confident that the described method will produce similar performance. Although proof for this is left for future work.

Chapter 4

Permanent Magnet Motors

There are two types of PMM, namely the brushless DC motor (BLDCM) and the permanent magnet synchronous motor (PMSM). Their strengths and weaknesses respectively have to be accounted for when deciding upon a suitable motor for a given application. Furthermore, the amount of phases, stator windings and magnetic poles may also vary according to requirements and application of the motor. Design criteria, such as stator stack skewing and type of rotor, must also be taken into account in order to optimize the motor for high performance applications [4]. A detailed account for all these parameters is an entire project by itself. This chapter will instead focus on the main characteristics of the PMM and recommend some fundamental design decisions for the project application at hand.

Before continuing, the reader should take note of the distinction between mechanical θ_m and electrical θ_{el} angles. It is a key concept that will be referred to throughout the rest of the report. The relation is dependent on the amount of magnetic poles, n_p , within the motor and can be expressed as

$$\theta_{el} = \frac{n_p}{2} \cdot \theta_m \quad (4.1)$$

4.1 Construction

In principle both PMM types operate by running current in a specific sequence through the stator winding, so called commutation. This creates a magnetic field that interacts with the permanent magnets fixed to the rotor, see Figure 4.1.

What differentiates the two motor types is how the stators are wound, resulting in different waveforms of the induced back electromotive force (back-emf) phase voltage. The

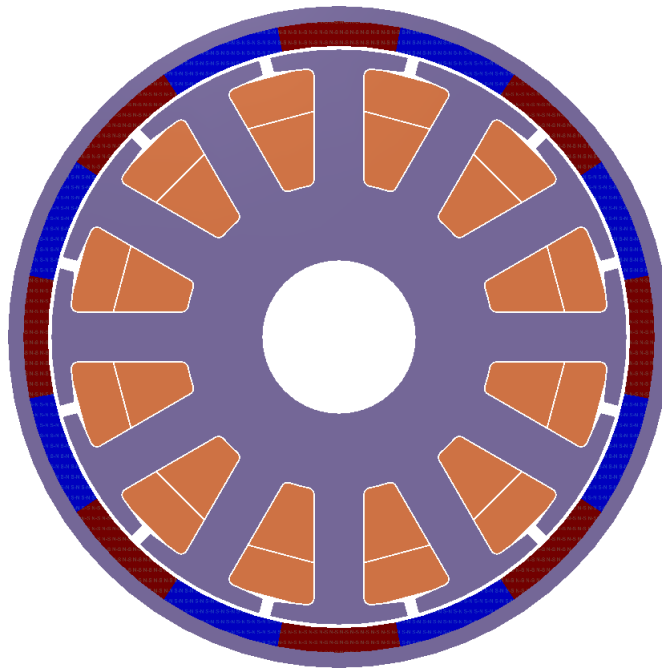


FIGURE 4.1: A cross section of a permanent magnet motor with an outer rotor.

stator winding of the BLDCM is concentrated, which in theory gives a trapezoidal shape of the back-emf waveform. In comparison, the PMSM phase windings are distributed in a manner that induces sinusoidal back-emf phase voltage, see Figure 4.2.

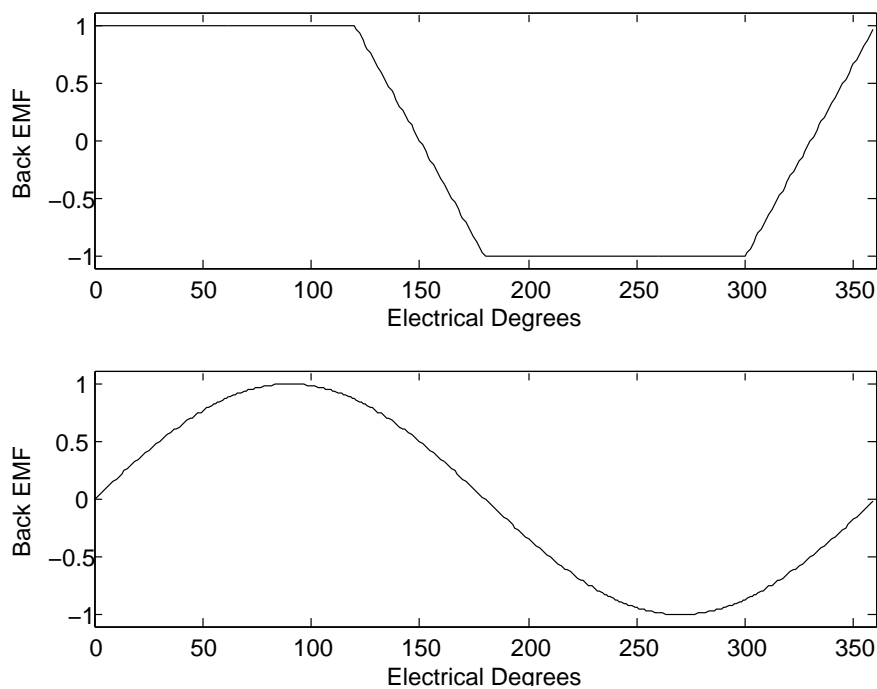


FIGURE 4.2: Ideal and normalized waveform of one phase of the induced back-emf for BLDCM (upper) and PMSM (lower).

The rotor can either be within the stator or outside of it. Naturally this affects the characteristics of the motor. Most significant of these is that the reluctance variation

between quadrature axes is fairly small for outer rotor motors. Resulting in direct and quadrature inductances being almost identical [5], see Chapters 6 and 7 for more in depth description of quadrature axis and its corresponding inductances. It is generally accepted that outer rotor motors are best suited for low velocity high torque applications, and vice versa for inner rotor motors [6].

The gross output torque is the sum of beneficial electromagnetic torque and unwanted torque produced by cogging, load, Coulomb friction and viscous friction. Of all unwanted effects the cogging torque is of most importance in low velocity applications. According to [4] one should choose either an 8 pole 9 slot motor or an 8 pole 18 slot motor for minimizing the effects of cogging. Furthermore skewing of stator stacks or magnets should be investigated.

4.2 Back Electromotive Force

Magnetic flux through a loop with area A in a magnetic field B is given by

$$\phi = BA \cos(\theta_{el}) \quad (4.2)$$

where $\theta = 0$ rad corresponds to a perpendicular angle towards the magnetic field. If the loop is wound N consecutive times, forming a stator coil, then ψ gives the total flux linkage of the stator according to

$$\psi = N\phi \quad (4.3)$$

According to Faraday's law of induction, the back-emf is defined as the negative time derivative of magnetic flux

$$e = -\frac{d\psi}{dt} = -N\frac{d\phi}{dt} = -N\frac{d\phi}{d\theta_{el}}\frac{d\theta_{el}}{dt} = -N\frac{d\phi}{d\theta_{el}}\omega_{el} = K_e\omega \quad (4.4)$$

where N is the number of loops of the coil, ϕ is the permanent magnet flux linkage, θ_{el} is the electric rotor angle and ω_{el} is the electric angular velocity and K_e is the back-emf constant defined as $[V \cdot \frac{s}{rad}]$. The negative sign of the back-emf is due to Lenz's law, which states that the induced emf generates a current that creates a magnetic field which opposes the change in magnetic flux.

As previously stated, the back-emf waveform of the PMM is dependent on its stator winding distribution. An ideal case of this waveform for each motor type is given in Equation 4.5 combined with Table 4.1.

TABLE 4.1: Function table for the ideal and normalized back-emf BLDCM.

Electric rotor angle θ_{el}	$f_a(\theta_{el})$	$f_b(\theta_{el})$	$f_c(\theta_{el})$
0°- 60°	1	-1	$1 - \frac{6\theta_r}{\pi}$
60°- 120°	1	$\frac{6\theta_r}{\pi} - 3$	-1
120°- 180°	$5 - \frac{6\theta_r}{\pi}$	1	-1
180°- 240°	-1	1	$\frac{6\theta_r}{\pi} - 7$
240°- 300°	-1	$9 - \frac{6\theta_r}{\pi}$	1
300°- 360°	$\frac{6\theta_r}{\pi} - 11$	-1	1

BLDCM: $e_i = K_e \omega_{el} f_i(\theta_{el})$, $i = \text{phases a, b and c}$

$$\text{PMSM: } \begin{cases} e_a = K_e \omega_{el} \sin(\theta_{el} - \frac{2\pi}{3}) \\ e_b = K_e \omega_{el} \sin(\theta_{el}) \\ e_c = K_e \omega_{el} \sin(\theta_{el} + \frac{2\pi}{3}) \end{cases} \quad (4.5)$$

4.3 Electromagnetic Torque

Torque produced in the PMSM is smooth due to the interaction between sinusoidal stator current and rotor flux. The same cannot be said for the BLDCM as smooth torque demands instantaneous and accurate phase commutation. This in turn is impossible due to the transient errors of the controlled current is unavoidable [7].

One solution to minimize the ripple in produced torque in BLDCM is to implement so called pseudo-vector control, effectively making the motor act as a PMSM. This requires a detailed mapping of the induced back-emf in a look-up table [7]. Although the technique looks promising, avoiding the BLDCM altogether seems to be the reasonable choice whenever it is possible.

4.4 Cost

As it is a difference in winding distribution that separates the two PMM types, cost of the actual motor is of no concern when comparing the two types. However, as the PMSM is vector controlled and the BLDCM usually is phase commutated, difference in control complexity is reflected in the necessary hardware for operating the two PMM types. Advancements in micro-controller technologies have made the cost of computing power of no concern.

4.5 Summary

The following design decisions are recommended for the given application:

1. PMSM with either an 8 pole 9 slot or an 8 pole 18 slot configuration for low torque ripple;
2. Outer rotor motor for low velocity and high torque;
3. Motor with skewed stator stacks or permanent magnets for reducing cogging torque.

Chapter 5

Prototype

5.1 Introduction

By eliminating the internal brushed commutator of the standard DC motor, the PMM is in need of an external control source for handling current commutation in the stator windings. The control source is in most cases a micro-controller unit (MCU). However, a CompactRIO from National Instruments [8][9] is utilized in the prototype developed for this project as it allows for an easy development environment for testing different control algorithms.

By sensing rotor position the controller coordinates the switching of a voltage source inverter (VSI) for commutation of motor phase windings. The VSI consists of one half-H bridge per motor phase. A greater understanding of the system dynamics is gained by implementing phase current sensing in addition to the position sensor. See Figure 5.1 for a block diagram overview of the prototype.

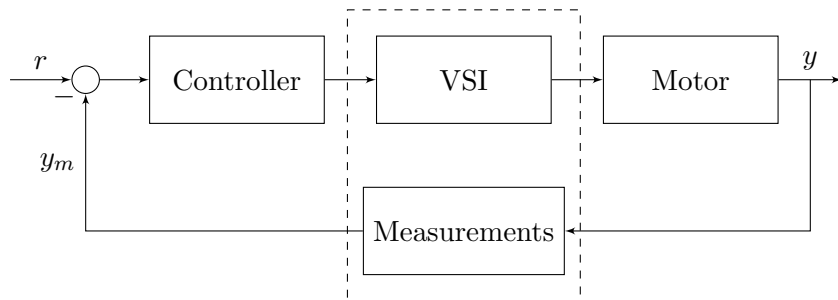


FIGURE 5.1: A block diagram of the prototype. Blocks within the dashed line are designed and implemented on a printed circuit board specifically for this project.

The rest of this chapter is dedicated to elaborating on each of the main components of the prototype. Figure 5.2 describes how these components interact. See Figure 5.3 for

5.2 Control Unit

From National Instruments (NI) a CompactRIO cRIO-9022 real-time controller (RT) together with a cRIO-9116 reconfigurable chassis housing a field-programmable gate array (FPGA) was used as control unit as it is versatile and powerful allowing freedom in control algorithm design. The RT has a 533 MHz Freescale MPC8347 real-time processor [8] and the FPGA is a Xilinx Virtex LX85 [9]. The FPGA clock runs at 40 MHz and the built in FPGA allows for running tasks in true parallel operation. The unit executes LabVIEW programs. To measure analog inputs a NI 9215 module with four channels with 16-bit 100 kHz simultaneous sampling [10] was used. The digital inputs and outputs were managed by two bi-directional NI 9401 modules each having eight channels with maximum 100 ns delay [11].

5.3 Software

The control software was programmed in both FPGA and RT. In Figure 5.4 the allocation of program functions is shown. Calculations in the FPGA were made in fixed-point arithmetic or integer. The RT has floating-point capability and calculations were, because of the reduced implementation complexity, made in floating point. Where to place the program functions were determined by the demand for fast execution and the need for accurate timing. The sections below describe the functions.

5.3.1 FPGA

PWM Controlling PWM outputs in VSI.

SPI Communication interface with rotary magnetic encoder chip for angular position.

Main Samples current and position, which are transformed from three phases a, b, c to two phase d, q . From the transformation the currents are controlled by feedback control. Controller outputs are transformed back to three phases which are then used to calculate the PWM duty cycles via a space vector modulation (SVM) function.

5.3.2 RT

Filtering 2^{nd} -order low pass filters for various filtering applications.

Control Feedback control of position and velocity.

Data logging Data logging used for troubleshooting, tuning and reporting.

UI The user interface (UI) enables the user to control the motor, adjust parameters and monitor the control and measurements.

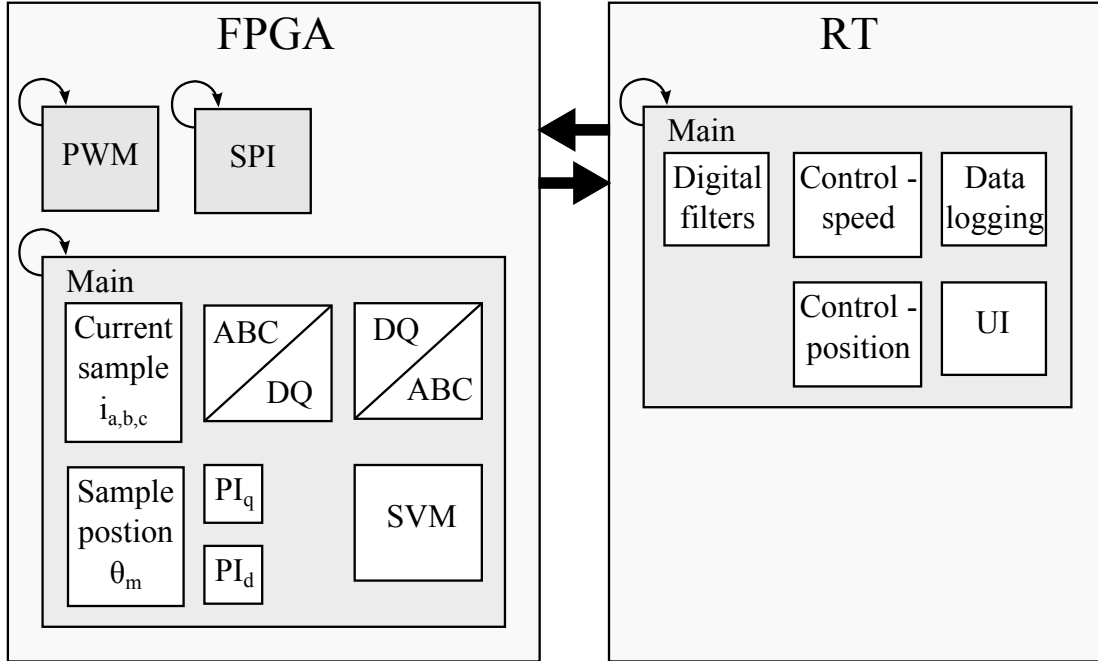


FIGURE 5.4: Program allocation on FPGA and RT, respectively.

5.3.3 Closed Loop Control

For control a traditional proportional integral (PI) controller was used with setpoint weighting and tracking to prevent windup of the integrator.

The discretized controller is shown in (5.1).

$$\begin{aligned}
 &\text{Proportional: } P_k = K(\beta y_{k,ref} - y_k), 0 \leq \beta \leq 1 \\
 &\text{Desired output: } v_k = P_k + I_{k-1} \\
 &\text{Limited output: } u_k = \begin{cases} v_{min} & \text{if } v_k \leq v_{min} \\ v_{max} & \text{else if } v_k \geq v_{max} \\ v_k & \text{else} \end{cases} \quad (5.1) \\
 &\text{Integral: } I_k = I_{k-1} + KT_s \left[\frac{1}{T_i} (y_{k,ref} - y_k) + \frac{1}{T_r} (u_k - v_k) \right]
 \end{aligned}$$

where K is feedback gain, β setpoint weighting, T_i integrator time constant, T_r output tracking time constant and T_s is the sampling time of the regulator

5.3.4 Implementation on Other Hardware

When programming a versatile system like the NI CompactRIO the aspect that a commercial implementation would be made on a low-cost MCU had to be taken into consideration. An FPGA is costly and is not likely to be used in a PTZ camera for motor control. The FPGA can however be excluded when implementing with a MCU. The reason is that an MCU has in most cases built-in hardware support for PWM and SPI. Transforming three phase to two phase will demand heavy trigonometric calculations. There are MCUs on the market with integrated digital signal processors (DSP) that will handle this transformation [12]. But implementation on conventional MCU is possible [13]. Operation performed in the RT can be programmed in fixed point arithmetic to facilitate implementation on an MCU. Parts of the program, such as data logging and UI, will not be needed in a commercial implementation and can be omitted.

5.4 Voltage Source Inverter

The phase commutation is handled by the integrated circuit (IC) DRV8332 from Texas Instruments [14]. The IC is a triple half-H bridge circuit, see Figure 5.5, with some added functionality, such as adjustable over-current protection as well as shoot-through prevention. Shoot-through occurs when both high and low sides of a half bridge are conducting current, thereby creating a short circuit. The IC is supplied with 12 VDC for logic and 24 VDC for the half bridges.

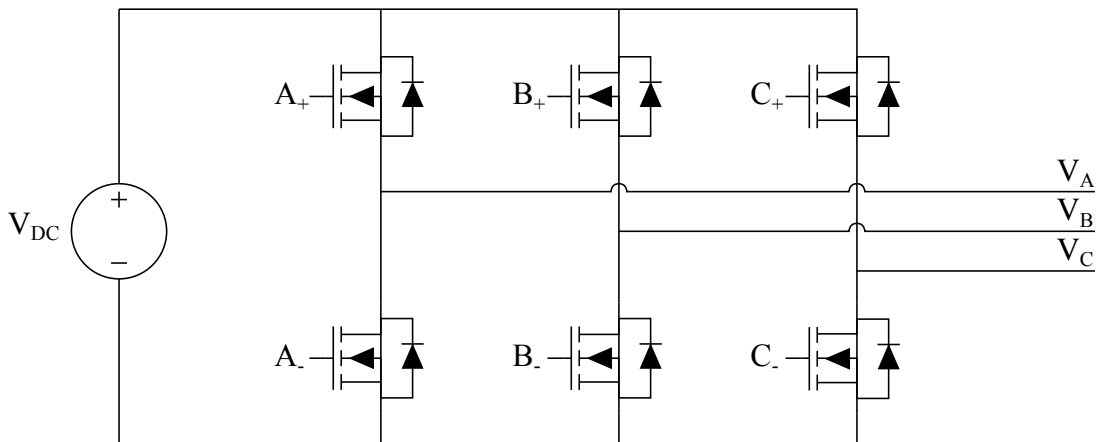


FIGURE 5.5: Principle of the triple half bridge.

5.5 Position Sensor

Rotor position measurement is done with a linear magnetic rotary encoder chip AS5311 [15]. A ring with 75 magnetic pole pairs is mounted on the outer rotor housing of the motor. From this ring the encoder chip uses its integrated hall effect sensors and digital signal processor to give an absolute position of 12 bit resolution within one pole pair giving in total 307200 steps on a complete revolution as shown in Figure 5.6. Sampling of the position was done by communication to the encoder chip via the serial peripheral interface (SPI) protocol.

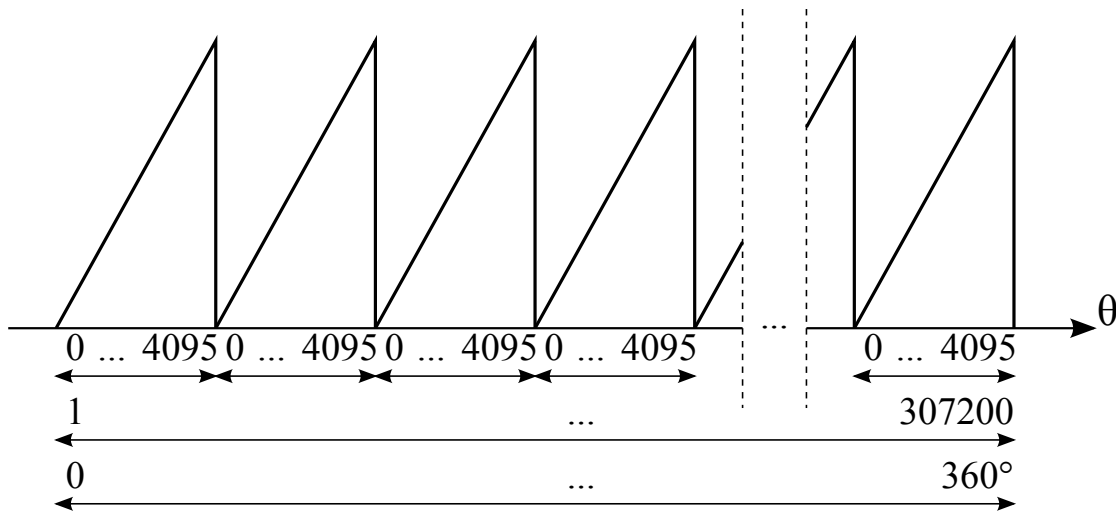


FIGURE 5.6: Position sensor scale.

Over a complete revolution the position is relative and only within a pole pair is the position absolute. In order to get absolute information of a full revolution the position was sampled fast enough to detect the change in magnetic pole pair and then make corrections of the total value accordingly.

Sampling rate was limiting the maximum rotational velocity that could be kept without losing track of position. Limitation is $2048 \text{ steps/sample}$ translating to a minimum of $150 \text{ samples/revolution}$. Running the SPI clock at 750 kHz and each sample was completed in 25 clock cycles resulted in a sampling rate of 30 kHz of the position giving a maximum velocity allowed to $200 \text{ revolutions/s}$.

The 307200 steps were degraded due to a noisy signal reading reducing the resolution by one fifth down to $61440 \text{ steps/revolution}$, which gives a resolution of $0.00585938^\circ/\text{step}$. The noisy signal is most likely due to an ambient magnetic field interfering with the measurement [15]. A moving average filter would most likely improve the performance at full resolution. However, it is left as future work.

5.6 Measuring Velocity

Motor angular velocity is differentiated from position as

$$\omega_m = \dot{\theta}_m \quad (5.2)$$

To measure the angular velocity discretization of (5.2) gives an estimation of angular velocity at sample k as

$$\omega_m(k) = \frac{\theta_m(k) - \theta_m(k-1)}{T_s} \quad (5.3)$$

where T_s is the sampling time.

Running at very low angular velocity imposes that the system cannot be sampled too often as a consequence of the finite resolution that the position measurement has. If sample rate is too high it results in

$$\theta_m(k) - \theta_m(k-1) = 0 \quad (5.4)$$

giving a reading $\omega(k)_m = 0$ even though the motor is rotating.

The ability to rotate smoothly at $0.05^\circ/s$ demands that the sensor needs to distinguish velocities lower than this for example one fifth of this value ($0.01^\circ/s$). This gives

$$\begin{aligned} \frac{1}{5} \cdot \frac{307200 \frac{\text{steps}}{\text{rev}}}{360^\circ/\text{rev}} &= \frac{512}{3} \text{steps}/^\circ \Rightarrow \\ \frac{512}{3} \text{steps}/^\circ \cdot 0.01^\circ/s &\approx 1.7 \frac{\text{steps}}{s} \end{aligned} \quad (5.5)$$

which results in a maximum sample rate of 1.7 Hz in order to sense the lowest velocity required. Added low-pass filtering reduced response even more.

5.7 Current Sensor

Current measurements can be done on the low side of each half-H bridge with a shunt resistor in the ground path of each half-H bridge. Typically the resistance is less than $50\text{m}\Omega$. The voltage drop over these resistances are amplified through differential amplifiers and then fed to the analog input of the controller. Low side positioning of current sense resistors is useful since it leads to low common mode voltage.

Evaluation of this method reveals one fundamental obstacle. The measured current is that of the half-H bridges and not the motor phases. Motor phase current is only equal to half-H bridge current if its low side transistor or freewheeling diode is conducting. A

sample and hold circuit must be implemented in order to reconstruct the signal when the low side is not conducting [16]. Matters still get more intricate since all phases should be sampled simultaneously in order to avoid phase-shift. This can only be achieved at zero vector state in the space vector modulation scheme utilized for switching the half-H bridges, see Chapter 8. The zero vector state is the only state where all three low sides are conducting simultaneously. The sample and hold circuit should be able to detect signals as short as 100 ns in length, which corresponds to the performance of the analog input module.

With limited time available work continued using hall effect sensors mounted directly on the motor phases [17]. See Table 5.1 for a review of the two sensing methods.

TABLE 5.1: Comparison of current sensing methods.

Current Sensing Method	Shunt Resistor	Hall Effect
Accuracy	Good	Good
Accuracy vs. Temperature	Good	Poor
Cost	Low	High
Isolation	No	Yes
High Current-Measuring Capability	Poor	Good
Saturation/Hysteresis Problem	No	Yes
Power Consumption	High	Low
Intrusive Measurement	Yes	No

When considering the attributes of each method, it is evident that the shunt resistor is superior. Cost is a key factor for product development. The product should be capable of operating in a wide range of temperatures and measurements should therefore not be dependent on temperature. High current capability is of no concern since measurements are done on low power motors. Power consumption is higher compared to Hall effect sensors however the difference is minuscule relative to total power consumption of the product. It can even be argued that the fact that current can be measured allows a more intelligent control of the motor since the motor does not draw current unless necessary.

5.7.1 Analog Current Filter

In order to reduce computation load on the controller an analog first-order low-pass filter was implemented with a resistor in series and a capacitor parallel to the load. The

cutoff frequency is given by

$$f_c = \frac{1}{2\pi RC} = \frac{1}{2\pi \cdot 10^3 \cdot 100 \cdot 10^{-9}} \approx 1.6 \text{ kHz} \quad (5.6)$$

The cutoff frequency is approximately 100 times higher than the highest steady state current frequency, thereby giving room for transient responses while at the same time effectively dampening unwanted noise.

5.8 Motor

The proposed recommendations for selecting the motor in section 4.5 has been taken into account when searching for a suitable model. However, the desired slot/pole configuration was not available at the time of ordering. Furthermore, few if any manufacturers provided information about skewing for minimizing cogging torque.

A motor from Maxon has been selected for this project [18]. It has an outer rotor and is reasonable in size. See Table 5.2 for motor specifications.

TABLE 5.2: Motor specification for Maxon EC45.

Motor Data	Value at nominal voltage
Nominal Voltage	24 [V]
Nominal Current	2.33 [A]
Nominal Torque	$83.4 \cdot 10^{-3}$ [Nm]
Torque Constant	$33.5 \cdot 10^{-3}$ [$\frac{Nm}{A}$]
Rotor Inertia	$1.35 \cdot 10^{-5}$ [$kg \cdot m^2$]

Careful consideration on how to dimension the actuator is an essential part of the project. In this section two alternative approaches to the problem will be investigated. The first approach use fundamental principles of physics to determine what torque is needed to rotate a camera in a manner that is deemed sufficient. The second approach is founded on choosing the most powerful motor that respects a certain power consumption restraint.

5.8.1 Necessary Torque Estimation

The camera can for simplicity be approximated as a solid sphere with a mass = 0.2 kg and radius = 0.05 m giving the load inertia as

$$J_{load} = \frac{2mr^2}{5} = 2 \cdot 10^{-4} \text{ [kg} \cdot \text{m}^2] \quad (5.7)$$

Taking into account the motor rotor inertia the total inertia becomes

$$J_{total} = J_{load} + J_{motor} = 2.135 \cdot 10^{-4} \quad [kg \cdot m^2] \quad (5.8)$$

According to Table 2.1 the system should be able to rotate half of one revolution in half a second. Assuming that positive and negative acceleration each constitute one half of the time needed for the movement gives a maximum acceleration of

$$\alpha_m = \frac{\Delta\omega_m}{\Delta t} = \frac{\Delta\theta_m}{(\Delta t)^2} = \frac{\pi}{2} \cdot 16 = 8\pi \quad \left[\frac{rad}{s^2}\right] \quad (5.9)$$

The theoretical torque needed to move the motor and load is given by

$$\tau = J_{total} \cdot \alpha_m \approx 5.4 \quad [\text{milli Nm}] \quad (5.10)$$

Compensation for error in estimated load inertia as well as friction and other phenomena is done by multiplying the theoretical torque with a safety factor K_s . This factor is usually around 1.5 to 2 [19], giving

$$\tau_{real} = K_s \cdot \tau = [8.1, 10.8] \quad [\text{milli Nm}] \quad (5.11)$$

However, for this project the safety factor is set much higher as it is undesirable for the motor to be the limiting factor in this early stage of prototype development. Having K_s around 10-20 gives a bound on the output torque as

$$\tau_{real} = K_s \cdot \tau = [54.0, 108.0] \quad [\text{milli Nm}] \quad (5.12)$$

5.8.2 Power Consumption Restraint

Consider a power consumption restraint of 3 W in continuous operation and 5 W in short term operation. Under the assumption that the motor phase to phase resistance is 1 Ω then current consumption becomes

$$\begin{aligned} I_{max} &= \sqrt{\frac{P_{max}}{R}} = \sqrt{\frac{5}{1}} = 2.23 \quad [A] \\ I_{cont} &= \sqrt{\frac{P_{cont}}{R}} = \sqrt{\frac{3}{1}} = 1.73 \quad [A] \end{aligned} \quad (5.13)$$

It is common for electric motor manufacturers to specify a so called torque constant, defined as $\left[\frac{Nm}{A}\right]$. It is desirable to select the motor with highest torque constant. In the

case of the Maxon EC 45 the torque output becomes

$$\begin{aligned}\tau_{max} &= K_{\tau} \cdot I_{max} = 74.9 \quad [\text{milli Nm}] \\ \tau_{cont} &= K_{\tau} \cdot I_{cont} = 58.0 \quad [\text{milli Nm}]\end{aligned}\tag{5.14}$$

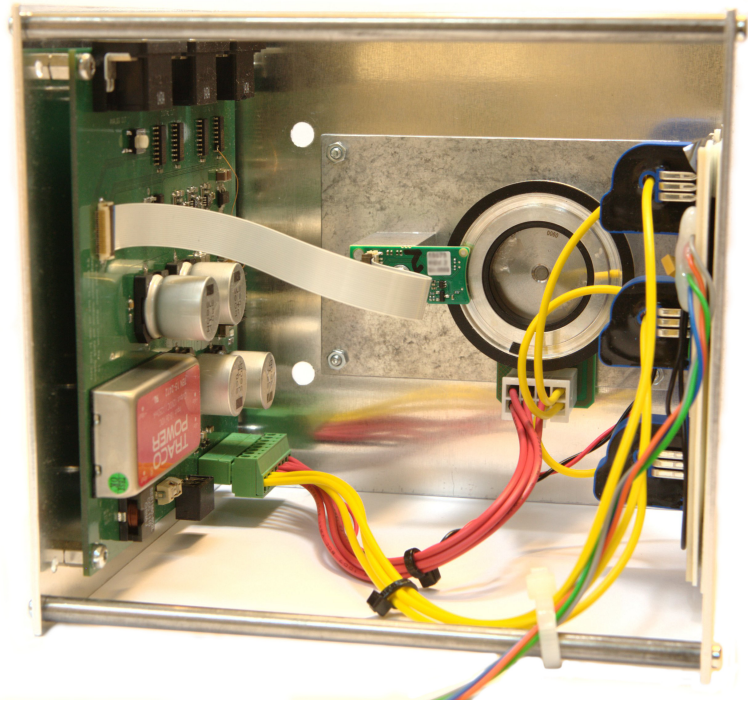


FIGURE 5.7: Full view of the prototype. The PCB is to the left, motor with position sensor in the middle and modified current sensing with hall sensors to the right.

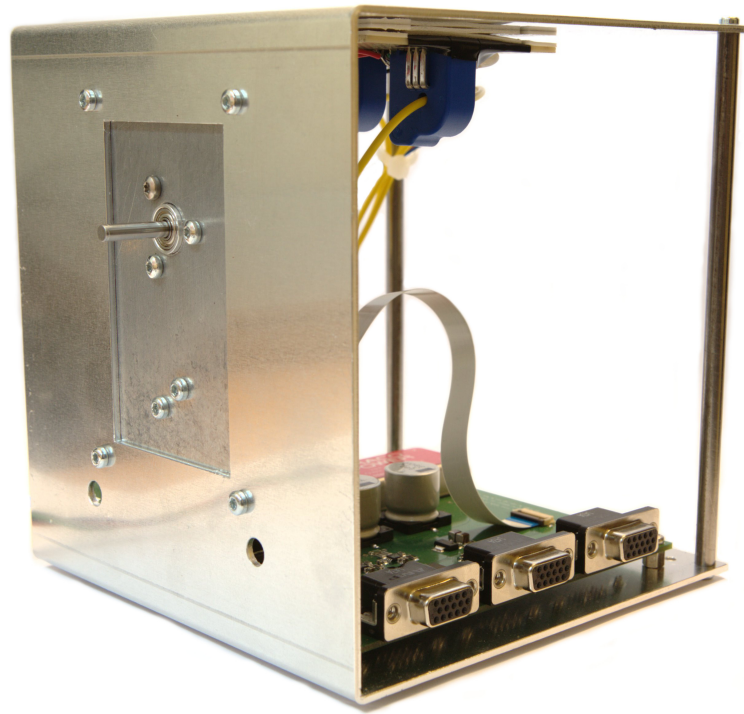


FIGURE 5.8: Front side of the prototype, this position simulates tilt motor control.

Chapter 6

Dynamic Modeling

6.1 Friction

In applications where tolerances on tracking errors are low and the demand for high precision positioning control is essential the effects of friction cannot be neglected. By modeling the friction it is possible to design a control system which can compensate for friction and therefore gain performance [20]. Friction can be modeled in several ways with dominating effects from Coulomb friction and viscous friction. Finer modeling can be made including the Striebeck effect.

6.1.1 Friction Model

In a motor the friction is a torque τ_f which relates to the torque τ produced by the motor as

$$\tau = J\dot{\omega} + \tau_f \quad (6.1)$$

where J is the moment of inertia and ω is the angular velocity. τ_f depends on ω and τ [21]. When $\omega = 0$ the friction is static. It can be modeled without dynamics as

$$\tau_f(0, \tau) = \begin{cases} \tau, & \text{if } |\tau| < k_s \\ k_s \text{sign}(\tau), & \text{if } |\tau| \geq k_s \end{cases} \quad k_s \text{ is the static friction constant} \quad (6.2)$$

When $\omega \neq 0$ the friction is no longer static. The friction is now kinetic and not depending on τ . Combining constant friction known as Coulomb friction and viscous friction the kinetic friction can be described as

$$\tau_{fk}(\omega) = k_c \text{sign}(\omega) + k_v \omega \quad (6.3)$$

where k_c is the Coulomb friction constant and k_v the viscous friction constant.

In the transition between static and Coulomb friction there is something known as Stribeck effect. To model this effect the Armstrong model can be used. Below this model is described [21].

$$\tau_{fk}(\omega) = \text{sign}(\omega)(k_c + (k_s - k_c)e^{-|\frac{\omega}{v_s}|^{\delta_v}}) + k_v\omega \quad (6.4)$$

where v_s is the Stribeck velocity coefficient and δ_v the fitting parameter.

To illustrate the differences of the models described in Equations (6.2), (6.3) and (6.4) the frictions torque function are plotted in Figure 6.1. Parameters used are $k_c = 0.15$, $k_s = 0.2$, $k_v = 0.005$, $v_s = 0.5$ and $\delta_v = 0.5$.

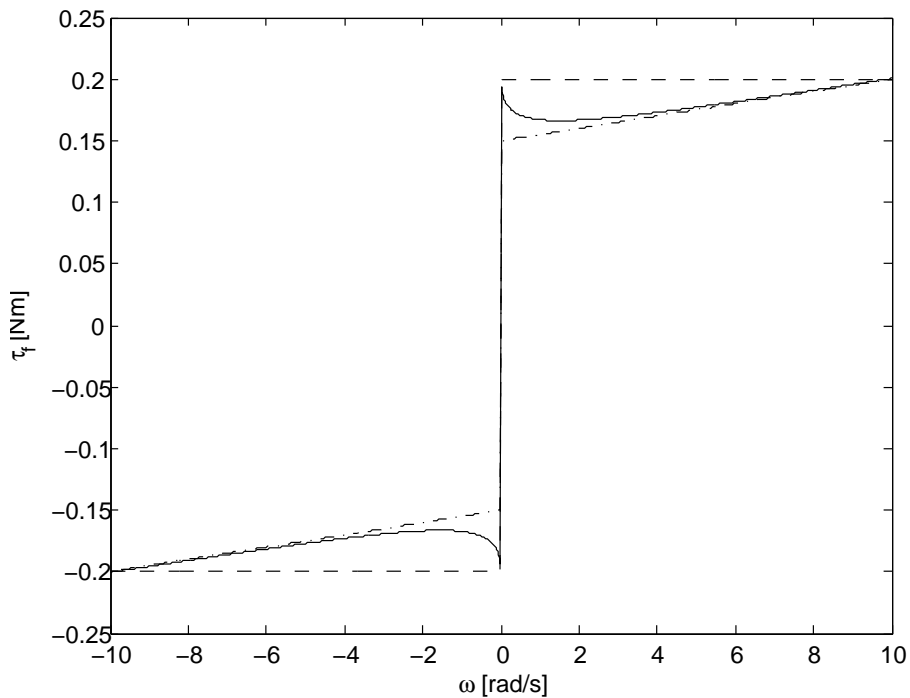


FIGURE 6.1: Illustrative plot of friction models. Dashed line: Coulomb friction. Dash-dotted line: Coulomb and viscous friction. Solid line: Coulomb and viscous friction with Stribeck effect.

From now on Equation (6.3) will be used to describe friction as it lends itself well for parameter identification and modeling.

6.2 Reference Frame Transformation

If it is desirable to control DC variables when the actual variables are sinusoidal, then considerable simplification of system equations are gained by using the rotor as reference frame for system variables.

A power invariant version of the transformation is according to [22] given by

$$\begin{pmatrix} d \\ q \\ 0 \end{pmatrix} = \sqrt{\frac{2}{3}} \begin{pmatrix} \cos(\theta_{el}) & \cos(\theta_{el} - \frac{2\pi}{3}) & \cos(\theta_{el} + \frac{2\pi}{3}) \\ -\sin(\theta_{el}) & -\sin(\theta_{el} - \frac{2\pi}{3}) & -\sin(\theta_{el} + \frac{2\pi}{3}) \\ \frac{\sqrt{2}}{2} & \frac{\sqrt{2}}{2} & \frac{\sqrt{2}}{2} \end{pmatrix} \begin{pmatrix} a \\ b \\ c \end{pmatrix} \quad (6.5)$$

and its corresponding inverse is given by

$$\begin{pmatrix} a \\ b \\ c \end{pmatrix} = \sqrt{\frac{2}{3}} \begin{pmatrix} \cos(\theta_{el}) & -\sin(\theta_{el}) & \frac{\sqrt{2}}{2} \\ \cos(\theta_{el} - \frac{2\pi}{3}) & -\sin(\theta_{el} - \frac{2\pi}{3}) & \frac{\sqrt{2}}{2} \\ \cos(\theta_{el} + \frac{2\pi}{3}) & -\sin(\theta_{el} + \frac{2\pi}{3}) & \frac{\sqrt{2}}{2} \end{pmatrix} \begin{pmatrix} d \\ q \\ 0 \end{pmatrix} \quad (6.6)$$

Under the assumption that the components always are balanced as $a+b+c=0$, which is true for no fault conditions, then the zero component can safely be ignored for increased computational efficiency. The reduced transform is then given by

$$\begin{pmatrix} d \\ q \end{pmatrix} = \sqrt{\frac{2}{3}} \begin{pmatrix} \cos(\theta_{el}) & \cos(\theta_{el} - \frac{2\pi}{3}) & \cos(\theta_{el} + \frac{2\pi}{3}) \\ -\sin(\theta_{el}) & -\sin(\theta_{el} - \frac{2\pi}{3}) & -\sin(\theta_{el} + \frac{2\pi}{3}) \end{pmatrix} \begin{pmatrix} a \\ b \\ c \end{pmatrix} \quad (6.7)$$

with its inverse counterpart given by

$$\begin{pmatrix} a \\ b \\ c \end{pmatrix} = \sqrt{\frac{2}{3}} \begin{pmatrix} \cos(\theta_{el}) & -\sin(\theta_{el}) \\ \cos(\theta_{el} - \frac{2\pi}{3}) & -\sin(\theta_{el} - \frac{2\pi}{3}) \\ \cos(\theta_{el} + \frac{2\pi}{3}) & -\sin(\theta_{el} + \frac{2\pi}{3}) \end{pmatrix} \begin{pmatrix} d \\ q \end{pmatrix} \quad (6.8)$$

An illustration of the transformation can be seen in Figure 6.2.

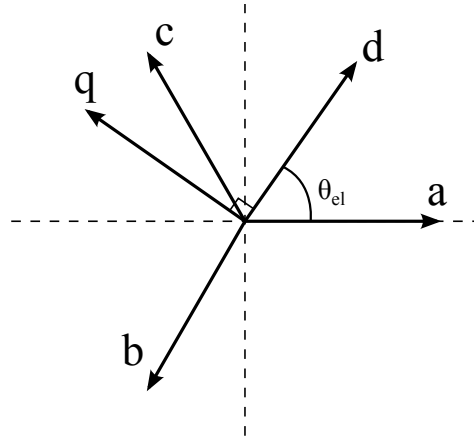


FIGURE 6.2: Visualization of the reference frame transformation.

6.3 System Equations

By knowing the amount of torque that is produced by the motor then other dynamics, such as rotor velocity and position, follows. Having a solid foundation in dynamic torque modeling is key to achieve high performance in the aforementioned areas.

The following assumptions have been made when developing the model; Reluctance torque is neglected since reluctance is for all intents and purposes independent of rotor position, see Table 7.2. Frequency dependence of stator resistance is disregarded since the motor is fed low frequency sinusoids. Core losses in magnetic materials of the machine are neglected as well as magnetic saturation. Temperature dependence mainly affects the permanent magnet flux linkage and as a consequence also the torque constant but also to some extent resistances and friction. According to [23], two-time-scale theory allows temperature to be considered constant in relation to the fast dynamics of the remaining system. The effect of temperature change will over time cause parameter drift. Finally, the torque load is only dependent on gravity and considered to only affect the tilt axis.

In the case of the electrical machine acting as a motor, the magnetic field induced by the stator always leads the permanent magnet rotor. The difference in angle is called torque angle (δ) and determines the fraction between direct and quadrature current as

$$\begin{aligned} i_d &= i_m \cos(\delta) \\ i_q &= i_m \sin(\delta) \end{aligned} \tag{6.9}$$

for the field-oriented control method described in Section 9.1 the direct current is forced to zero as $\delta = \pm \frac{\pi}{2}$ rad whereas direct and quadrature currents are coupled in synchronous

control as described in Chapter 10. The benefit of having a torque angle of 90 degrees is that it gives maximum torque output per input current, see Figure 6.3.

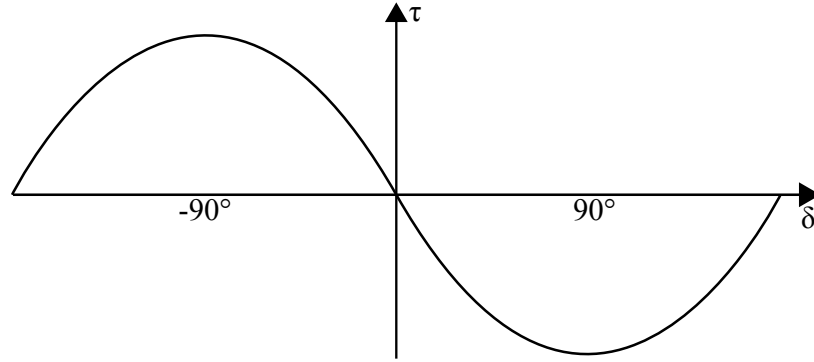


FIGURE 6.3: Electromagnetic torque output as a function of torque angle.

The rotor reference also transforms the real stator-windings to its fictitious counterparts, resulting in the two inductances L_d and L_q that are independent of rotor position. According to [5] and [23], the electrical model of the PMSM in rotor reference frame is given by

$$\begin{pmatrix} v_d \\ v_q \end{pmatrix} = \begin{pmatrix} R + pL_d & -\omega_{el}L_q \\ \omega_{el}L_d & R + pL_q \end{pmatrix} \begin{pmatrix} i_d \\ i_q \end{pmatrix} + \begin{pmatrix} 0 \\ \omega_{el}K_e \end{pmatrix} \quad (6.10)$$

where p is the derivative operator. Multiplying the left hand side of Equation (6.10) with its respective current and converting to mechanical velocity gives the instantaneous input power of the machine as

$$\begin{aligned} P &= v_d i_d + v_q i_q \\ &= R[i_d^2 + i_q^2] + (L_d i_d \frac{di_d}{dt} + L_q i_q \frac{di_q}{dt}) + \frac{n_p}{2} \omega_m i_q ((L_d - L_q) i_d + K_e) \end{aligned} \quad (6.11)$$

where $R[i_d^2 + i_q^2]$ represents the resistive losses over the stator and $L_d i_d \frac{di_d}{dt} + L_q i_q \frac{di_q}{dt}$ is the rate of change of stored magnetic energy. The last component, $\frac{n_p}{2} \omega_m i_q ((L_d - L_q) i_d + K_e)$, is synonymous with the electromagnetic power. Dividing the last component in Equation (6.11) with the mechanical rotor velocity gives the electromagnetic torque as

$$\tau_e = \frac{n_p}{2} i_q ((L_d - L_q) i_d + K_e) \quad (6.12)$$

Since an outer rotor motor is used and $L_d \approx L_q$, see Section 7.2, the electromagnetic torque function can safely be approximated as

$$\tau_e = \frac{n_p}{2} K_e i_q \quad (6.13)$$

A mechanical model including friction described in Equation (6.3) for the PMSM can be formulated as

$$\frac{d\omega_m}{dt} = \frac{1}{J} \left(\frac{n_p}{2} \tau_e - \text{sign}(\omega_m) k_c - k_v \omega_m - \tau_l + \tau_c \right) \quad (6.14)$$

where τ_l is load torque, τ_c is cogging torque, k_c is the Coulomb friction constant and k_v is the viscous friction constant. Combining Equation (6.12) with Equation (6.14) gives

$$\frac{d\omega_m}{dt} = \frac{1}{J} \left(\frac{n_p}{2} K_e i_q - \text{sign}(\omega_m) k_c - k_v \omega_m + \tau_l + \tau_c \right) \quad (6.15)$$

where torque load is defined as

$$\tau_l = -r m g \cos(\theta_m) \quad (6.16)$$

where r is the radius from axis of rotation to center of mass m and g is gravitational acceleration, θ_m is defined as the angle between the rotor and horizontal plane. The cogging torque is implemented in a look-up table, see Section 7.4. Now every state of the process can be expressed as

$$\begin{aligned} \frac{di_d}{dt} &= \frac{1}{L_d} (v_d + L_q \omega_{el} i_q - R i_d) \\ \frac{di_q}{dt} &= \frac{1}{L_q} (v_q - R i_q - L_d \omega_{el} i_d - K_e \omega_{el}) \\ \frac{d\omega_m}{dt} &= \frac{1}{J} \left(\frac{n_p}{2} K_e i_q - \text{sign}(\omega_m) k_c - k_v \omega_m + \tau_l + \tau_c \right) \\ \frac{d\theta_m}{dt} &= \omega_m \end{aligned} \quad (6.17)$$

The System Equations in (6.17) form the basis for a *MathWorks Simulink* simulation of the continuous closed loop system in Section 9.2.

Chapter 7

Parameter Identification

In order to simulate the process a number of parameters needed to be identified. Most of them were not accounted for in the motor specification and the ones that were was measured for the purpose of validation. Parameter measurements of the PMSM in Sections 7.1, 7.2 and 7.3 were done according to the methodology described in [24].

7.1 Phase Resistance

The phase to neutral resistance of the motor is according to the data-sheet 515 m Ω . A four-terminal measurement has been performed in order to verify this claim, see Table 7.1. The device used in measuring the phase resistance is rated at 1.0 % accuracy in the given range and is considered more accurate than the rated value in the data-sheet since it lacks information of measurement uncertainty.

TABLE 7.1: Four-terminal measurement of phase to neutral resistance.

Type	Value
Phase A resistance	496 m Ω
Phase B resistance	492 m Ω
Phase C resistance	483 m Ω
Mean phase resistance	490 m Ω

7.2 Direct and Quadrature Inductance

According to [24], as the rotor is aligned and locked with either $\theta_{el} = 0$ or $\theta_{el} = \frac{\pi}{2}$, a step in voltage creates a current response that is equivalent to a first order RL circuit:

$$i_{d,q} = \frac{V}{R}(1 - e^{-\frac{t}{\tau_{d,q}}}), \quad \tau_{d,q} = \frac{L}{R} \quad (7.1)$$

where L is the total inductance for the connection of the stator windings, which gives

$$L_d = \frac{2}{3}L, \quad (\theta_{el} = 0) \quad (7.2)$$

$$L_q = \frac{2}{3}L, \quad (\theta_{el} = \frac{\pi}{2}) \quad (7.3)$$

$$L_{d,q} = \frac{2}{3}\tau_{d,q}R \quad (7.4)$$

In order to reduce the impact of measurement noise, a function generator was used to repeatedly generate the voltage step. A bank of capacitors was added in order for the supply voltage to cope with the sudden surge of current. The circuit is shown in Figure 7.1. The measurement reading is an average of one thousand steps of these voltage steps. See Figure 7.2 for plots of the measurements.

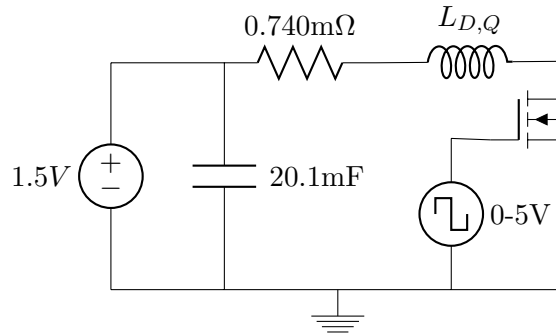


FIGURE 7.1: Circuit diagram for measuring current step responses of L_d and L_q .

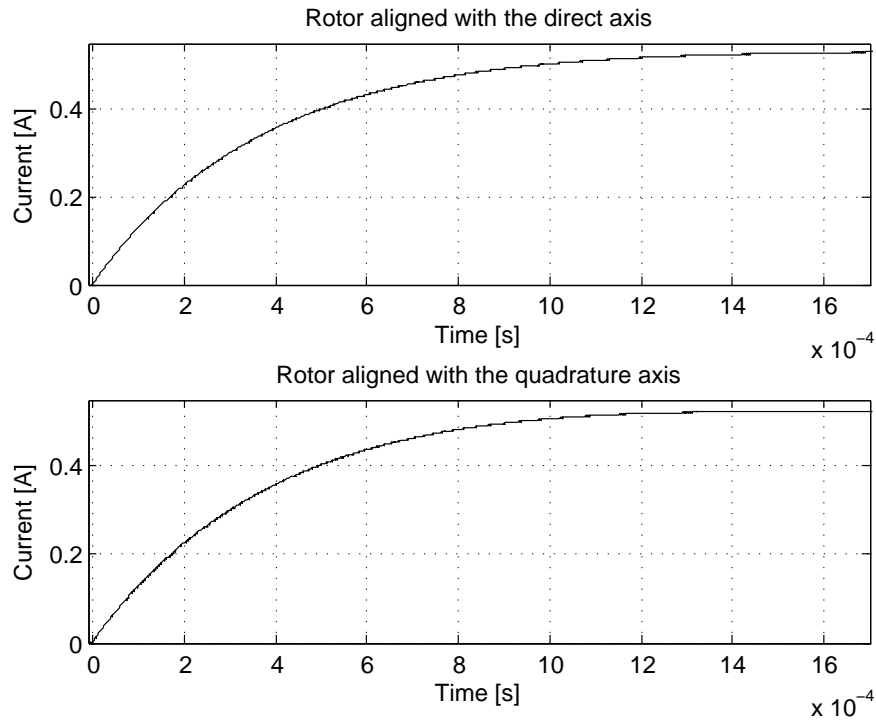


FIGURE 7.2: Measurements of a voltage step response with an amplitude of 1.5 V. The current responses are in both cases typical of the first order RL circuit. Both inductances have clearly reached their final level after 1.5 ms.

As both measurements were done with phase a in series with phase b and c in parallel, the total resistance over the stator windings including motor cables is $R = 740 \text{ m}\Omega$. The rise time 0-63.2% was measured as $\tau_d = 359.7 \text{ }\mu\text{s}$ and $\tau_q = 349.6 \text{ }\mu\text{s}$. See Table 7.2 for the measured value of the d and q inductances in accordance with Equation (7.4).

TABLE 7.2: Measured values of direct and quadrature inductances.

Type	Value
Direct inductance L_d	$176.37 \text{ }\mu\text{H}$
Quadrature inductance L_q	$171.42 \text{ }\mu\text{H}$

Their close resemblance in value is due to the fact that the motor has a surface mounted permanent magnet hence reluctance is roughly the same in every position [24].

7.3 Back-emf & Torque Constant

Induced motor voltage due to electromotive force increases linearly with angular velocity and its slope is determined by the back-emf constant. The back-emf constant is equivalent to the torque constant $[\frac{Nm}{A}]$. It is a parameter that is often listed in motor data sheets and is of practical use when determining the relation between input current and produced torque. The relation is

$$\frac{V \cdot s}{rad} = \frac{kg \cdot m^2}{A \cdot s^2} = \frac{N \cdot m}{A} \quad (7.5)$$

A test for measuring the back-emf constant was done by driving the PMSM at a constant velocity and measuring the phase to neutral voltage. An angular velocity controlled DC motor with a gearbox with ratio 53:1 drove the PMSM as a generator. See Figure 7.3 for induced voltage measurements at 130 rpm.

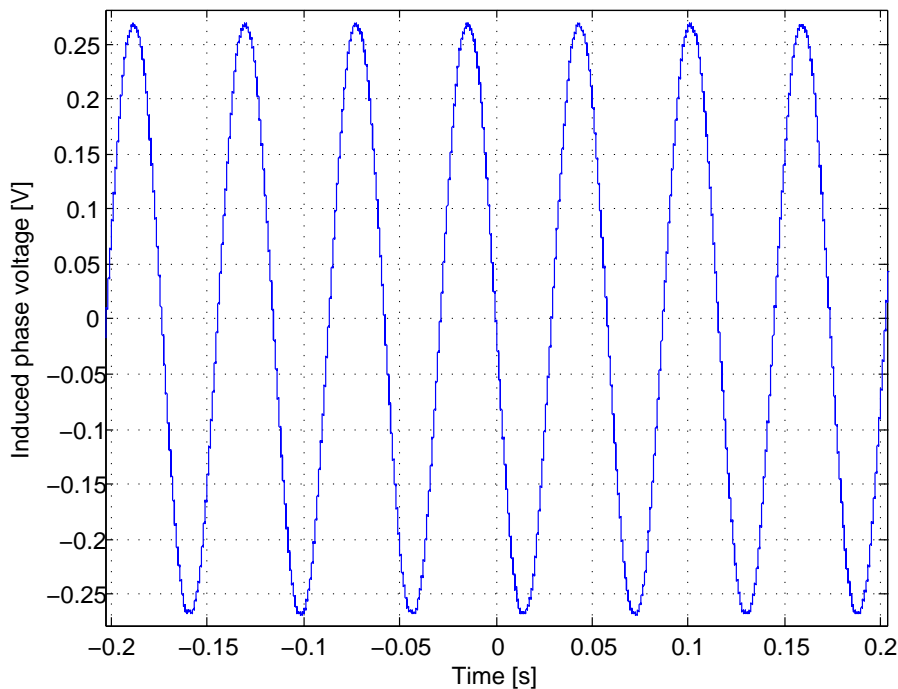


FIGURE 7.3: Induced phase voltage at 130 rpm. Peak to peak voltage is 535 mV and the period is 57.8 ms.

Data acquired in Figure 7.3 gives the back-emf K_e according to

$$K_e = \frac{V_{pk}}{\omega_{el}} = \frac{V_{pk-pk}}{2\omega_{el}} = \frac{V_{pk-pk}T}{4\pi} = 2.46 \cdot 10^{-3} \frac{V \cdot s}{rad} \quad (7.6)$$

By converting K_e to mechanical angular velocity and compensating for the phase to neutral voltage gives the torque constant as

$$K_t = \frac{n_p}{2} \cdot \sqrt{3} \cdot K_e = 34.0 \cdot 10^{-3} \quad \left[\frac{N \cdot m}{A} \right] \quad (7.7)$$

This validates the value of $K_t = 33.5 \cdot 10^{-3} \frac{N \cdot m}{A}$ that is specified in the datasheet. The relatively low induced voltage makes measurement errors introduced by the voltage probe more significant, as such the torque constant value listed in the datasheet is considered more reliable. For use in the dynamic model, the torque constant listed in the datasheet is converted to its back-emf counterpart

$$K_e = \frac{2}{n_p} \cdot \frac{1}{\sqrt{3}} \cdot 33.5 \cdot 10^{-3} = 2.42 \cdot 10^{-3} \quad \left[\frac{V \cdot s}{rad} \right] \quad (7.8)$$

7.4 Cogging Torque

All PM motors suffer to some extent from the unwanted effect of cogging torque. It is a byproduct of the interaction between the permanent magnet rotor and stator windings. The effect is predominately evident at low angular velocity in low inertia systems and is therefore one of the main concerns when high precision position control is desired.

There are several different models for analytical prediction of this phenomena. All of them require detailed knowledge of the motor at hand and their validity for different motor types are subject to research [25]. Another approach is to do a finite element analysis on the motor at hand. Lastly there is identification by experimental measurement as this circumvents complex calculations or simulations as described in [26]. Although this method of identification looks promising it requires a torque transducer, which was not available at the time. This project will therefore only evaluate simulated parameters, see Section 11.3.2.

7.5 Friction Parameter Identification

Running at a constant velocity and using (6.15), $\frac{d\omega_m}{dt} = 0$ and $\tau_l = \tau_c = 0$ leaves

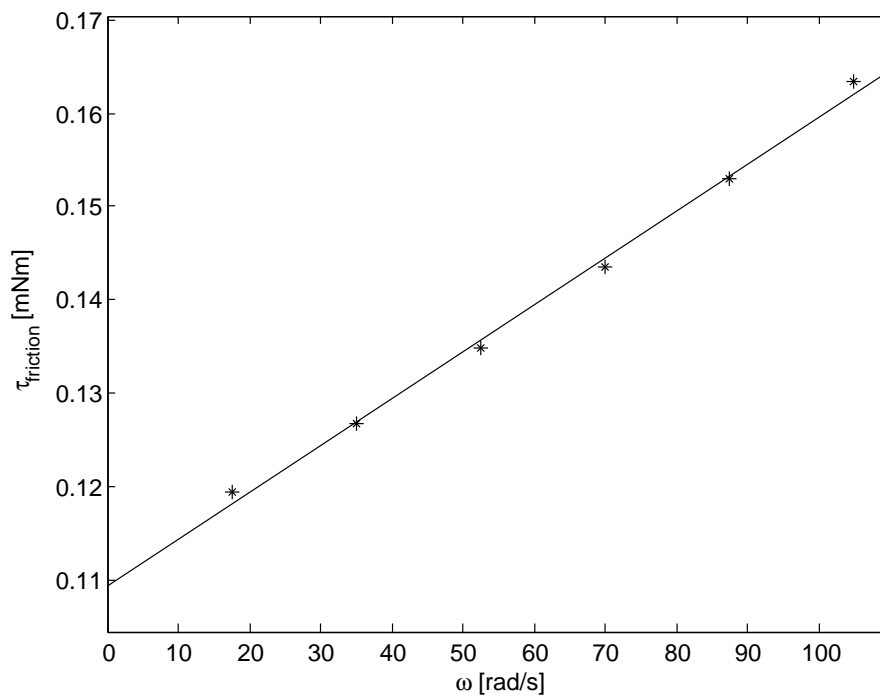
$$0 = \frac{1}{J} \left(\frac{n_p}{2} K_e i_q - \text{sign}(\omega_m) k_c - k_v \omega_m \right) \quad (7.9)$$

Sufficient angular velocity is required to reduce the effect of cogging torque. The inertia of the system will average cogging torque to $\tau_c = 0$.

Measuring the current i_q at various angular velocities then the torque produced can be calculated with Equation (6.13). Given the data linear interpolation can be performed, see Figure 7.4. In Table 7.3 the result is shown.

TABLE 7.3: Measured values of friction constants.

Type	Value
Viscous friction constant k_v	$0.50 \cdot 10^{-6} \text{ kg}\cdot\text{m}^2/\text{s}$
Coulomb friction constant k_c	$0.11 \cdot 10^{-3} \text{ Nm}$

FIGURE 7.4: Friction torque measured at different angular velocities to identify friction parameter constants k_v and k_c .

Chapter 8

Space Vector Modulation

To generate sinusoidal phase currents to drive the motor Space Vector Modulation (SVM) has been implemented. SVM has proven to have low current harmonics compared to the method of generating sinusoidal currents with sampled sinusoidal reference [27]. SVM is also a well-established method and has become a standard for power converters [28].

8.1 Principle of Operation

The concept of SVM is that the three phase voltage references $v_{a,ref}, v_{b,ref}, v_{c,ref}$ are transformed into two phase stator coordinates $v_{\alpha,ref}$ and $v_{\beta,ref}$ [29] which in their turn can be represented by a voltage reference vector $\mathbf{v}_{0,ref}$.

The three half-bridges in the VSI, see Figure 5.5, can in total accomplish eight switching vectors shown in Table 8.1. In Figure 8.1 the vectors are shown in $\alpha\beta$ -coordinates together with a voltage reference in Sector I. With these eight vectors it is possible to generate any voltage reference which is inside the hexagon. To modulate $\mathbf{v}_{0,ref}$ zero vectors $\mathbf{V}_z = \mathbf{V}_0 = \mathbf{V}_7$ and the two adjacent active vectors \mathbf{V}_i and \mathbf{V}_j are used. In Equation (8.1) $\mathbf{v}_{0,ref}$ is expressed as a linear combination of the three vectors $\mathbf{V}_z, \mathbf{V}_i, \mathbf{V}_j$.

$$\mathbf{v}_{0,ref} = d_z \mathbf{V}_z + d_i \mathbf{V}_i + d_j \mathbf{V}_j \quad (8.1)$$

The duty cycles are given in equation (8.2) where $m = \sqrt{3} \frac{|v_{0,ref}|}{v_{DC}}, 0 \leq m \leq 1$.

$$\begin{aligned} d_i &= m \sin \frac{\pi}{3} - \theta_r \\ d_j &= m \sin \theta_r \\ d_z &= 1 - d_i - d_j \\ 0 &\leq \theta_r \leq \frac{\pi}{3} \end{aligned} \tag{8.2}$$

Zero vector duty cycle is derived as equation (8.3).

$$d_0 = d_7 = \frac{d_z}{2} \tag{8.3}$$

TABLE 8.1: Switching table for SVM.

Vector	A^+	B^+	C^+	A^-	B^-	C^-	v_{ab}	v_{bc}	v_{ca}	
$\mathbf{V}_0 = 000$	Off	Off	Off	On	On	On	0	0	0	Zero Vector
$\mathbf{V}_1 = 100$	On	Off	Off	Off	On	On	$+v_{DC}$	0	$-v_{DC}$	Active Vector
$\mathbf{V}_2 = 110$	On	On	Off	Off	Off	On	0	$+v_{DC}$	$-v_{DC}$	Active Vector
$\mathbf{V}_3 = 010$	Off	On	Off	On	Off	On	$-v_{DC}$	$+v_{DC}$	0	Active Vector
$\mathbf{V}_4 = 011$	Off	On	On	On	Off	Off	$-v_{DC}$	0	$+v_{DC}$	Active Vector
$\mathbf{V}_5 = 001$	Off	Off	On	On	On	Off	0	$-v_{DC}$	$+v_{DC}$	Active Vector
$\mathbf{V}_6 = 101$	On	Off	On	Off	On	Off	$+v_{DC}$	$-v_{DC}$	0	Active Vector
$\mathbf{V}_7 = 111$	On	On	On	Off	Off	Off	0	0	0	Zero Vector

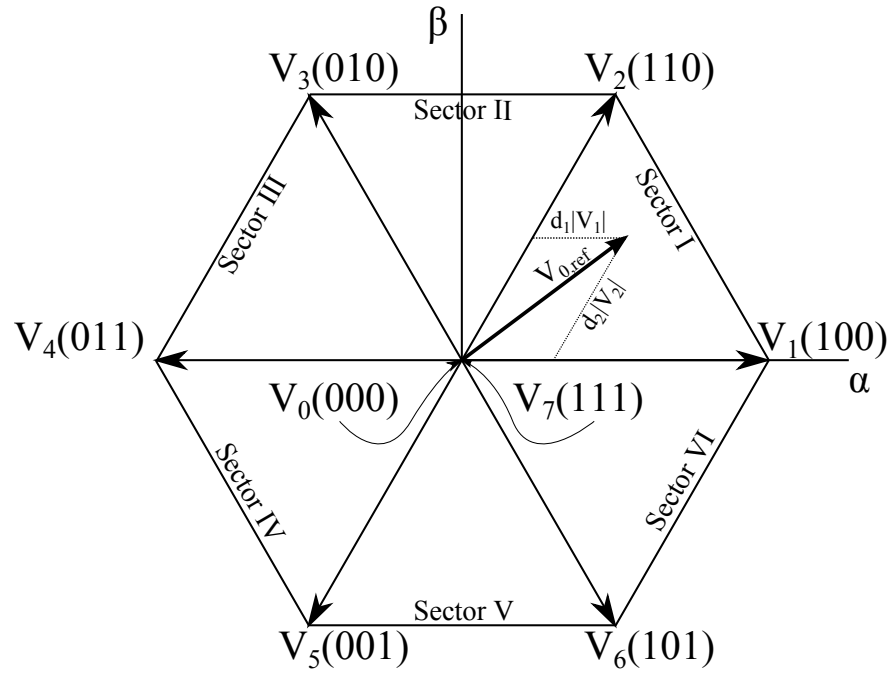


FIGURE 8.1: VSI space vectors with reference voltage vector $\mathbf{v}_{0,ref}$ in Sector I. Active vectors \mathbf{V}_i , $i = 1, \dots, 6$ are separated by $\frac{\pi}{3}$. d_1 and d_2 are duty cycles for voltage vectors \mathbf{V}_1 and \mathbf{V}_2 , respectively.

To avoid the computational heavy trigonometric functions in Equation (8.2) a method suggested in [30] was used, see Algorithm 1. It is easy and straight forward to implement and requires less computational effort suitable for implementation on micro controllers.

Algorithm 1 SVM duty cycle generation

```

1:  $v_{ab} = v_a - v_a, v_{bc} = v_b - b_c, v_{ca} = v_c - v_a$ 
2: if  $v_{ab} \geq 0$  then
3:   if  $v_{bc,ref} \geq 0$  then # Sector I
4:      $d_i = \frac{1}{v_{dc}}v_{ab}, V_i = V_1$ 
5:      $d_j = \frac{1}{v_{dc}}v_{bc}, V_j = V_2$ 
6:   else if  $v_{ca,ref} \geq 0$  then # Sector V
7:      $d_i = \frac{1}{v_{dc}}v_{ca}, V_i = V_5$ 
8:      $d_j = \frac{1}{v_{dc}}v_{ab}, V_j = V_6$ 
9:   else # Sector VI
10:     $d_i = -\frac{1}{v_{dc}}v_{ca}, V_i = V_1$ 
11:     $d_j = -\frac{1}{v_{dc}}v_{bc}, V_j = V_6$ 
12:  end if
13: else
14:   if  $v_{bc,ref} < 0$  then # Sector IV
15:      $d_i = -\frac{1}{v_{dc}}v_{bc}, V_i = V_5$ 
16:      $d_j = -\frac{1}{v_{dc}}v_{ab}, V_j = V_4$ 
17:   else if  $v_{ca,ref} < 0$  then # Sector II
18:      $d_i = -\frac{1}{v_{dc}}v_{ab}, V_i = V_3$ 
19:      $d_j = -\frac{1}{v_{dc}}v_{ca}, V_j = V_2$ 
20:   else # Sector III
21:      $d_i = \frac{1}{v_{dc}}v_{bc}, V_i = V_3$ 
22:      $d_j = \frac{1}{v_{dc}}v_{ca}, V_j = V_4$ 
23:   end if
24: end if
25:  $d_z = 1 - d_i - d_j$ 

```

8.2 Switching Sequence

There are several ways to arrange the switching sequence. Several of them are described in [28]. The Symmetric generated SVM seen in Figure 8.2 was used as a balance of implementation complexity and performance.

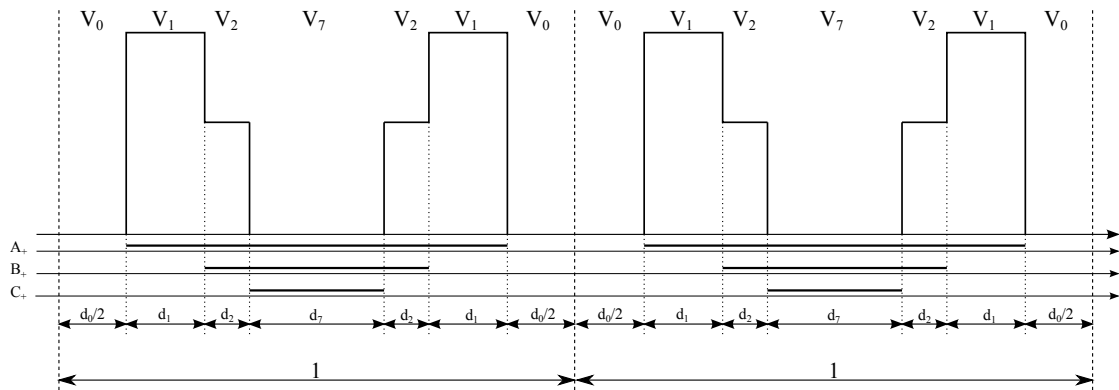


FIGURE 8.2: Method for generating symmetric SVM. Here operating in Sector I.

Chapter 9

Field-Oriented Control

9.1 Theory

By use of Equation (6.5) current control can be done with the DC currents i_d and i_q instead of AC currents i_a, i_b and i_c , which enables faster torque control. As a result of Equation (6.12) being reduced to Equation (6.13) i_q is the only current that produces torque. Since i_d does not add any torque it is natural that $i_{d,ref} = 0$. By forcing $i_d = 0$ by means of current control the torque angle is $\delta = 90^\circ$ at all time. This configuration enables position control as in Figure 9.1. Position control gives an angular velocity reference to the angular velocity controller which in its turn outputs an acceleration reference which is proportional to the torque and hence the current i_q . The reference of torque is controlled by the i_q current controller. Through this cascade coupling of controllers a double integrator is achieved that transforms the position reference to an acceleration, which can be controlled by regulating the current feed to the motor.

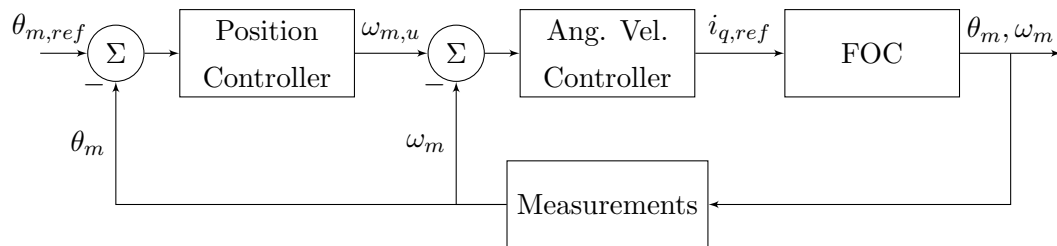


FIGURE 9.1: Position and angular velocity control in cascade coupling.

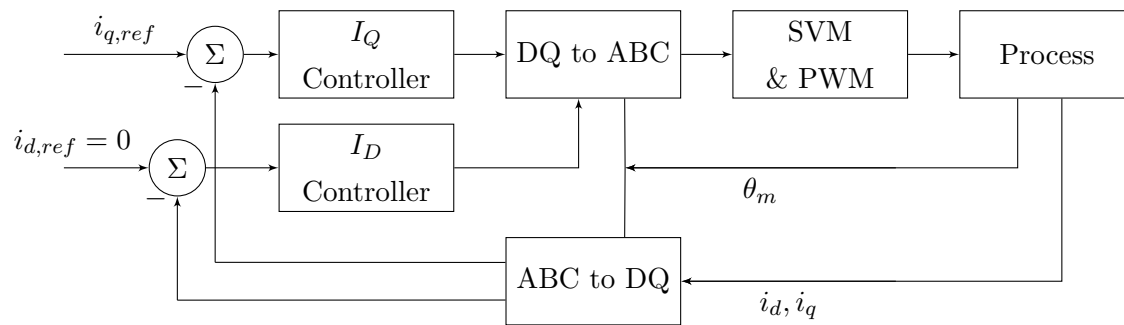


FIGURE 9.2: Contents of the FOC block in Figure 9.1. The process constitutes both the voltage source inverter and motor.

In this control scheme the inner loop seen in Figure 9.2 can run at a high sample frequency ($f_s = 10$ kHz) gaining very high bandwidth. The two outer loops will in their turn have a lower sample frequency but still with a relatively good bandwidth.

The control method described above is a common way to control an electric motor.

9.2 Simulation

The performance of the control law is evaluated with a position step response of 180 degrees. In Figure 9.3, position and angular velocity measurements are shown. The rise time is promising when comparing to the half second criteria for a step according to Table 2.1.

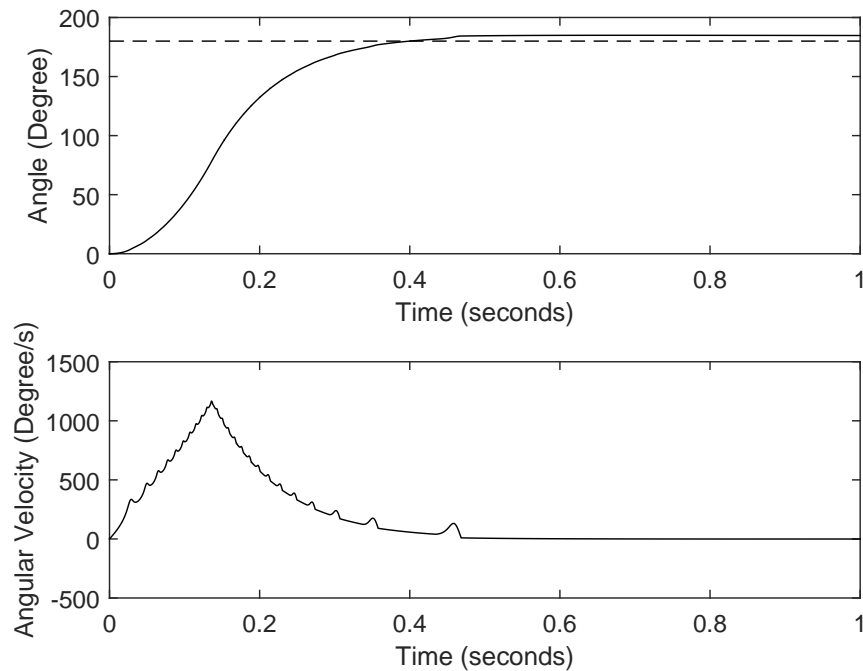


FIGURE 9.3: Angle and angular velocity response. Rise time from 10 % to 90 % is about 228 milliseconds. There is a steady state error in position of 4.8 degrees.

Total power consumption in Figure 9.4 shows that the controlled system exceeds the maximum power consumption only during short transients. These power transients are due to the large rate of change in stored magnetic energy described by the second term in Equation (6.11). The time duration for each and every one of them is less than one millisecond and the largest peak is approximately 30 W, therefore the energy content is of no concern when selecting capacitors for the drive circuit.

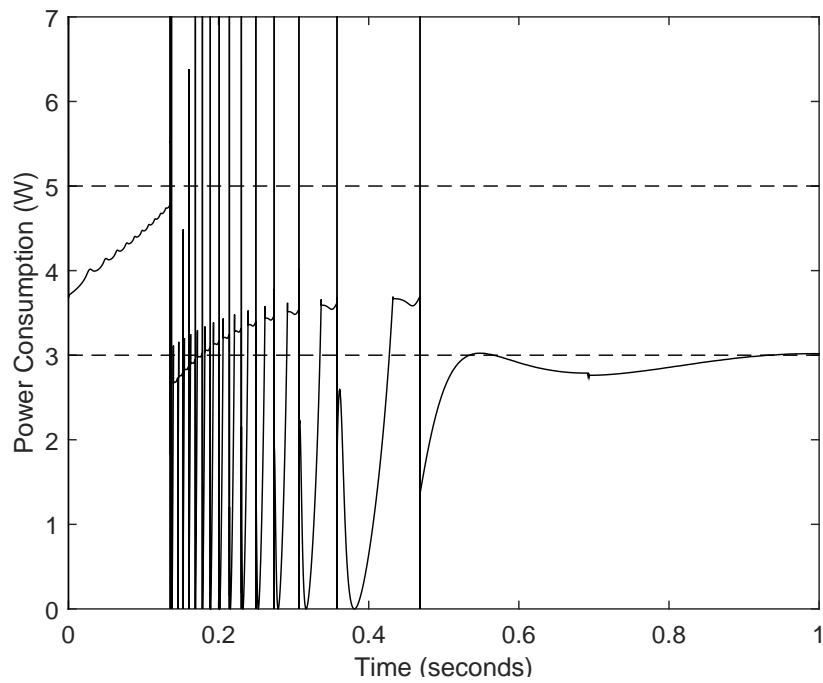


FIGURE 9.4: Total instantaneous power consumption during the step and five and three watts limits are marked.

In Figure 9.5 the benefit of applying current control in the rotor reference frame is apparent. Each sign change in quadrature current causes a change in sequence of the three phase currents.

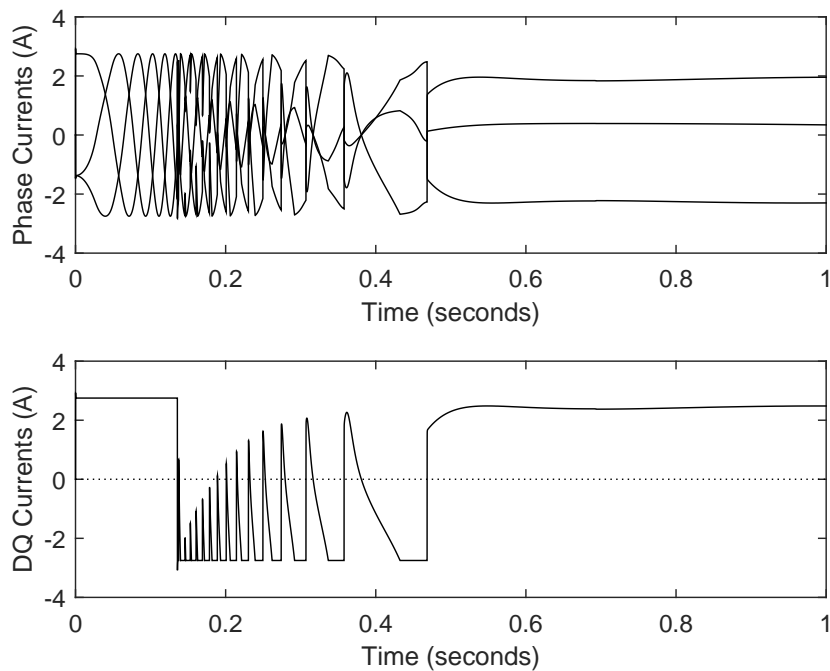


FIGURE 9.5: The lower plot shows direct current (dotted) and quadrature current (line). Sign change in quadrature current causes a change in sequence for the three phase currents in the upper plot.

Figure 9.6 illustrates the difficulties involved with controlling the system as the gross torque acting on the system is highly dynamic.

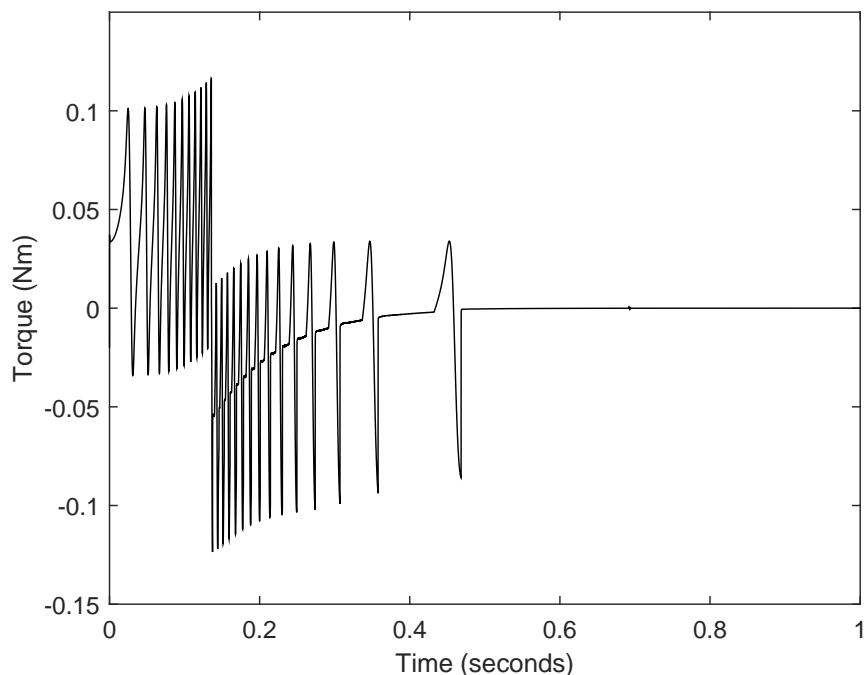


FIGURE 9.6: Gross torque acting on the system..

The simulated controller was discretized in order to determine how fast the system needs to be sampled for achieving sufficient bandwidth. As it turns out the angular velocity needs a sampling rate of 3.5-8 kHz for stable position or very low velocity control. If the position encoder had a factor of 400-1000 more steps per revolution it would be possible to sample at the simulated rate. Such an extremely high resolution encoder would in turn either limit the maximum angular velocity or require even higher sampling of the position in order not to miss a change in magnetic pole pairs on the encoder ring.

9.3 Results

9.3.1 Step Response Angle

Position control was not possible to achieve with any satisfactory performance. In Figure 9.7 a step response from $0 - 180^\circ$ is shown. Angular velocity controller and the torque controlled by i_q are seen in Figures 9.8 and 9.9, respectively. The position controller struggles to reduce the error to zero. Problems occur when the angular velocity controller is not able to operate under a certain velocity. Position error is integrated giving a ramp angular velocity reference. Angular velocity control is not able to respond to the low reference values. When the torque produced is large enough to overcome friction and cogging torque the motor will move. The amplitude of the resulting torque is so great that the position control overshoots. At some point a rather stable position at $t = [9, 13]s$ is found but there is still some error giving a reference to the angular velocity controller $\omega_{ref} \neq 0$ which in its turn integrates to be able to respond to the commanded velocity. This again results in position overshoot. The behavior originates from the angular velocity controller. Running at very low angular velocity is not possible without modifying the control method.

Even though steady state error is significantly higher than the system requirements it is worth noting that the rise time of the initial movement is less than one second.

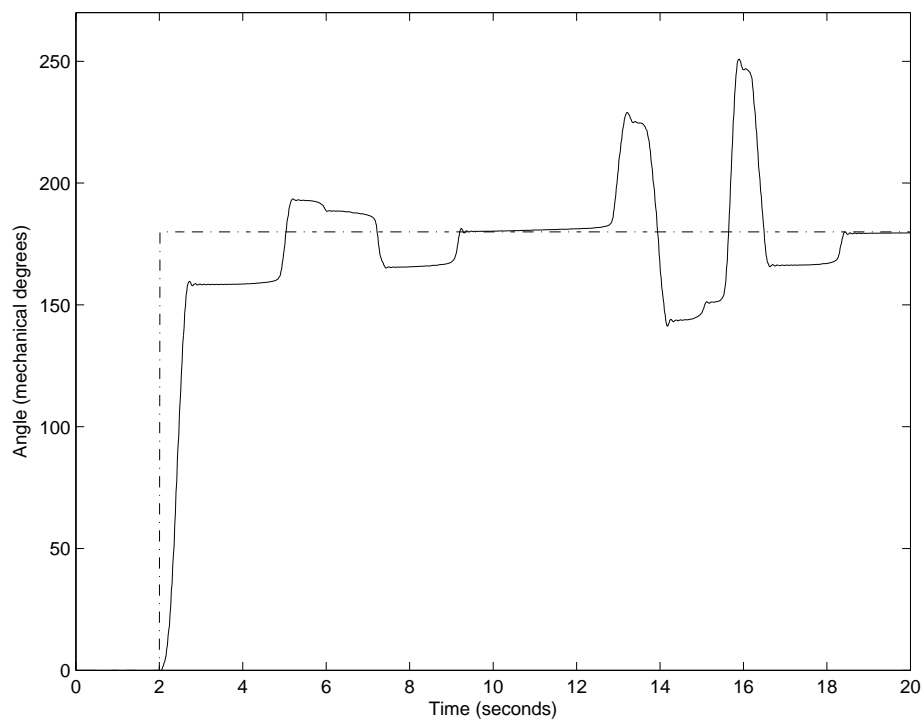


FIGURE 9.7: Position step 0-180°. The dot-dashed line is position reference and the continuous line is position measurement.

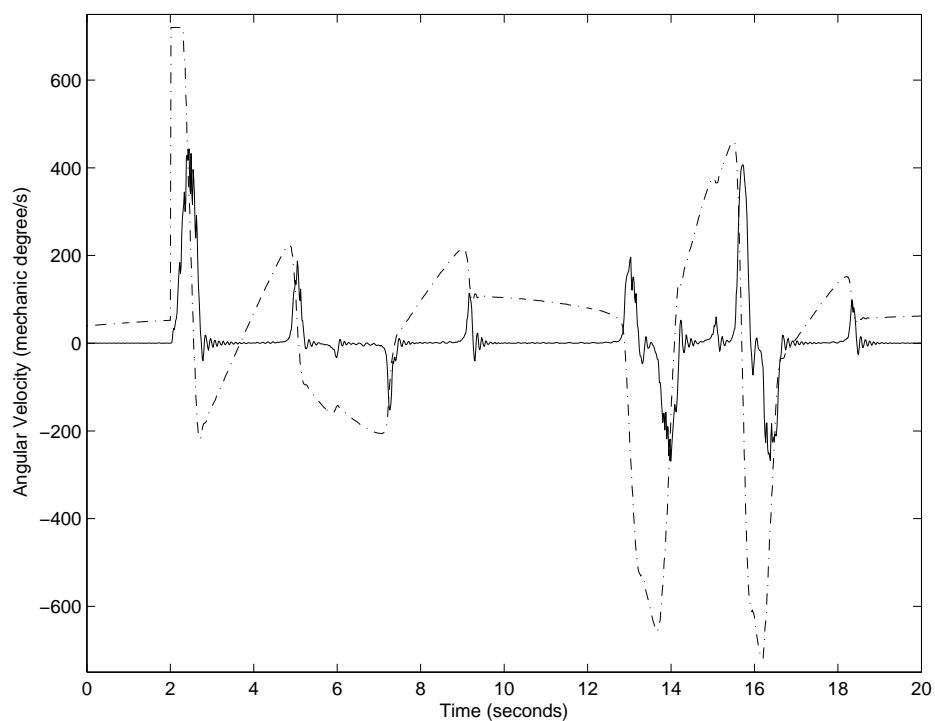


FIGURE 9.8: Velocity control during position step 0-180°. The dot-dashed line is velocity reference and the continuous line is velocity measurement

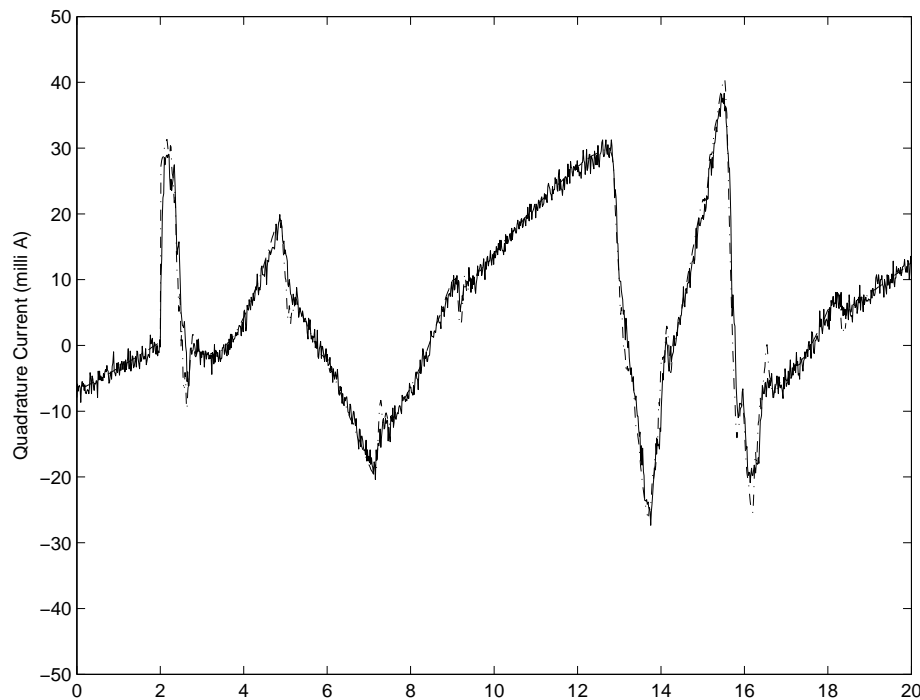


FIGURE 9.9: Current control during position step 0-180°. The dot-dashed line is quadrature current reference and the continuous line is quadrature current measurement

9.3.2 Constant Low Angular Velocity

Running at very low angular velocity as low as $0.05^\circ/s$ is not possible in this configuration. Problems with measuring angular velocity described in Section 5.6 becomes evident when trying to control at low velocity. Sampling the angular velocity at 20 Hz it was possible to run at $90^\circ/s$ which is 1800 times faster than the slowest operation point specified as critical. Lowering the sample rate even further to measure even slower angular velocity was pointless as cogging and friction torque prohibits very low angular velocity operation. In previous Section 9.3.1 results show poor performance at low angular velocity. The bandwidth of the angular velocity controller is not sufficient to compensate for the nonlinear behavior that the cogging and friction torque contributes to the system.

9.3.3 Step Response Angular Velocity

This control method have been successfully implemented for angular velocities higher than $360^\circ/s$. In Figures 9.10 and 9.11, a step response of angular velocity control is shown. The angular velocity controller was sampled at 32.25 Hz.

During operation at $360^\circ/s$ it can be seen that the velocity oscillates with 1 Hz. The cause is not related to the control. Possible causes are uneven friction during the revolution or that the position sensor suffers from a nonlinearity.

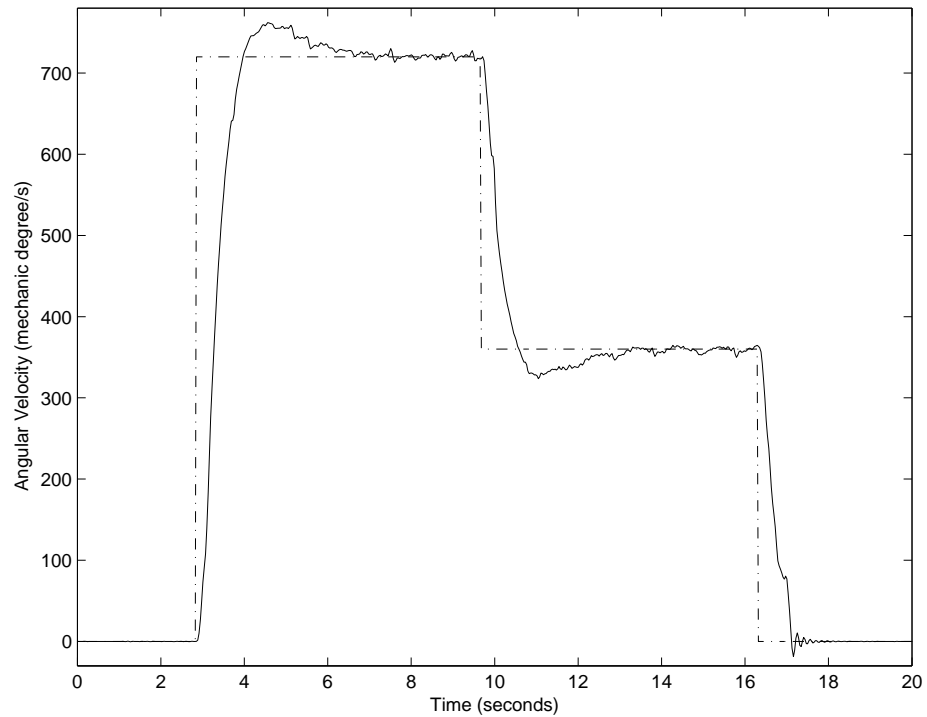


FIGURE 9.10: Speed step response $0 - 720 - 360 - 0^\circ/s$. Dashed line is controller set point and solid line is measured value.

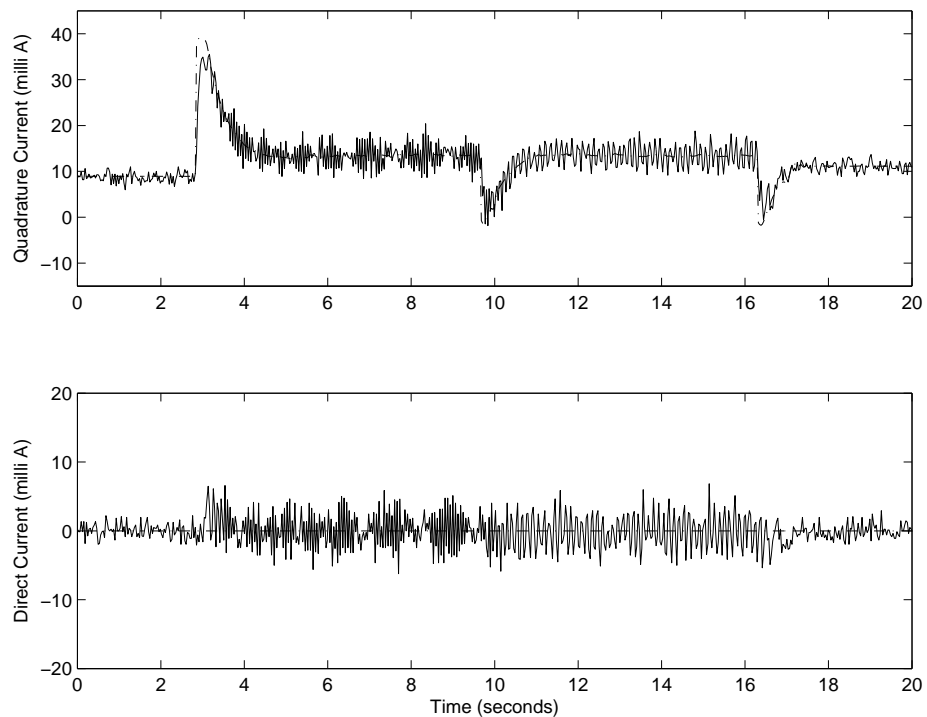


FIGURE 9.11: Currents i_q and i_d during the velocity step response $0 - 720 - 360 - 0^\circ/s$. Dashed line is controller set point and solid line is measured value

Chapter 10

Synchronous Control

An interesting phenomena was observed during software testing and debugging of the DQ-transform, SVM and PWM blocks. When feeding the motor with a constant quadrature current and at the same time increasing the angle fed into the DQ-transform and its inverse counterpart, a considerably slower rotation was achieved compared to what later would be achieved with the field-oriented control. Naturally the rotation was not smooth since the process was open loop, but a precedence had been set to continue investigating the performance in closed loop. Simulation of this control law was omitted since successful operation on the prototype was near at hand.

10.1 Theory

In principle, the controller varies the offset angle between induced magnetic field and permanent magnet rotor instead of forcing it to ± 90 degrees as in constant torque angle control. It is a moderate solution that is less sensitive to load disturbances. In return however it is slower in response of reference changes as the torque angle has to ramp up from a stable low value for each position step response. Of note is that the resulting torque angle should never exceed 90 degrees or else rotor slipping would occur. This could either be solved by implementing a tracking feature for limiting the control output or, as in this case, by low pass filtering the position reference.

Further work with the idea led to the following control scheme, see Figure 10.1 for a main level block diagram and Figure 10.2 for the inner current control loop in detail.

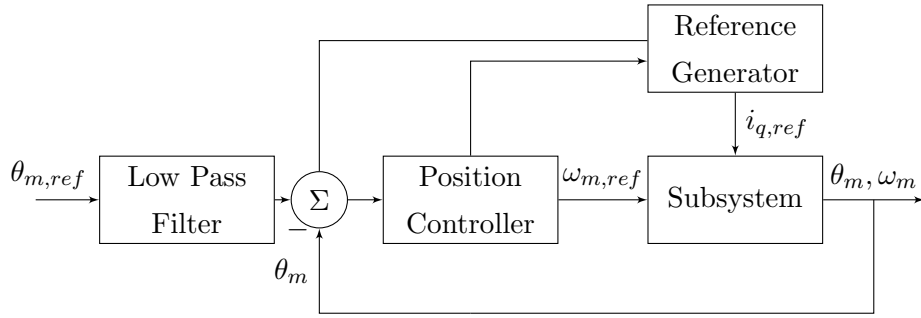


FIGURE 10.1: General structure of the synchronous controller.

The reference generator gives the quadrature current as

$$i_{q,ref} = |\theta_{m,error}| \cdot K_{error} + |\omega_{m,ref}| \cdot K_{\omega}$$

$$i_{q,ref} = \begin{cases} 0.1, & \text{if } i_{q,ref} < 0.1 \\ 0.2, & \text{if } i_{q,ref} \geq 0.2 \end{cases} \quad (10.1)$$

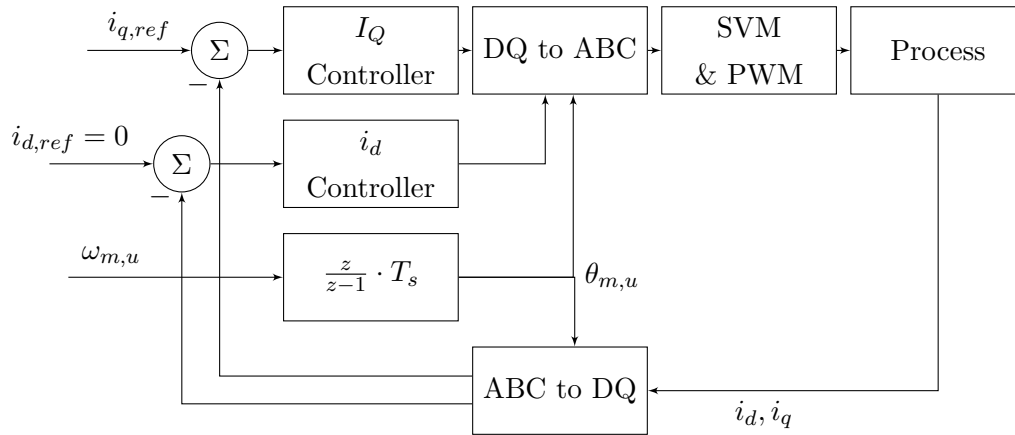


FIGURE 10.2: Contents of the subsystem block. The process constitutes both the voltage source inverter and motor.

It is intuitive to think that there should be an induced magnetic field present as long as there exists a position error and/or a velocity reference in order for actuation of the rotor. Even if there exists no such signal there still needs to be a lower limit on the quadrature current otherwise load disturbances would interfere. The upper limit ensures that power consumption remains within reason.

10.2 Results

The results in this section has been gathered with the main loop and data logger running at 125 Hz. The step responses are done in panning mode making the load unbalance of little or no significance on the measurement.

10.2.1 Step Response Angle

In Figure 10.3 a position measurement is shown. Rise time is considerably slower than the simulated step for field-oriented control. Furthermore with an error band of ± 1 degree the settling time is 2.5 seconds with no overshoot. The lowest possible angle that could be differentiated from zero is 5.9 milli-degrees and as such numerical errors are present in the data processing. The steady state error is still considered excellent as it is well below the positional accuracy of 0.1 degrees listed in the system requirements.

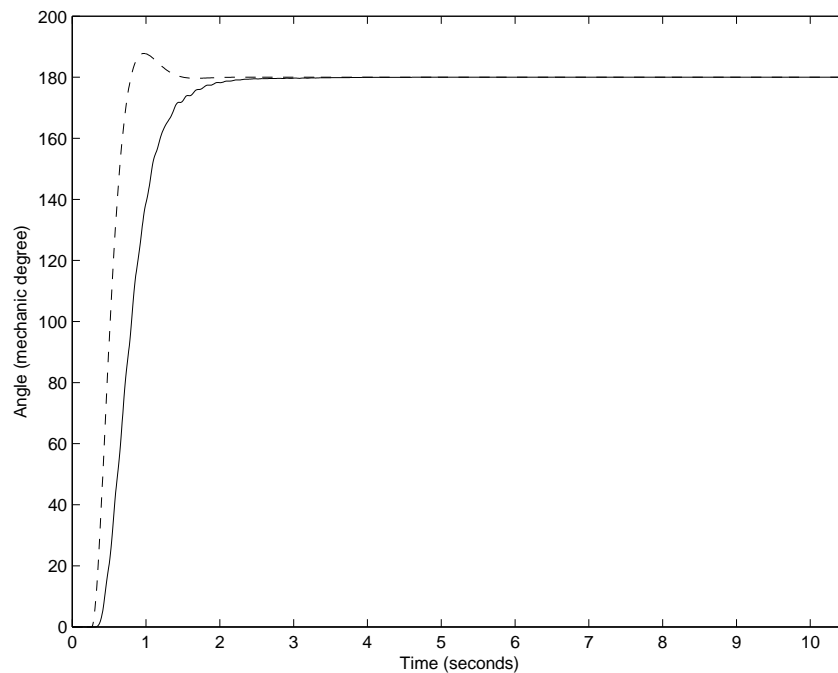


FIGURE 10.3: Filtered step reference (dashed) and rotor angle (line). Rise time from 10 % to 90 % is 0.74 seconds and steady state error is 0.001 degrees.

In Figure 10.4 quadrature current reference adapts as described in Equation (10.1). When steady state is achieved current is once again lowered corresponding to a minimum holding torque value.

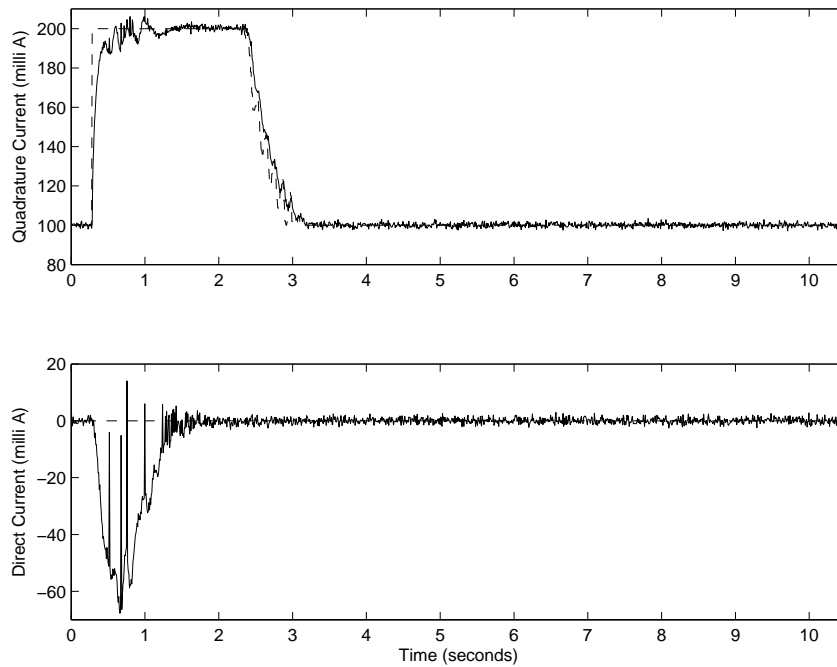


FIGURE 10.4: The current reference (dashed) and measurement (line) for direct and quadrature current.

The benefit of this control method is clearly visualized in Figure 10.5. As steady state position is achieved torque angle simply rises to compensate for the lowered quadrature current. This offloading is possible to a maximum of 90 degrees before slipping occurs.

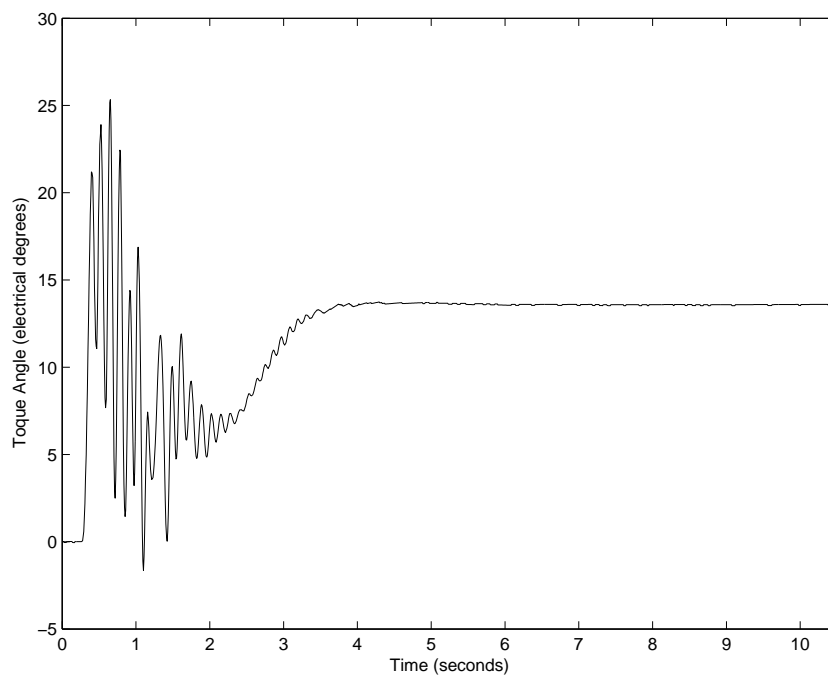


FIGURE 10.5: Resulting torque angle from the interaction between stator field and rotor magnetic field.

10.2.2 Constant Low Angular Velocity

When running the angular velocity control in open loop the performance meets the specified minimum rotation velocity set in the system requirements, see Figure 10.6.

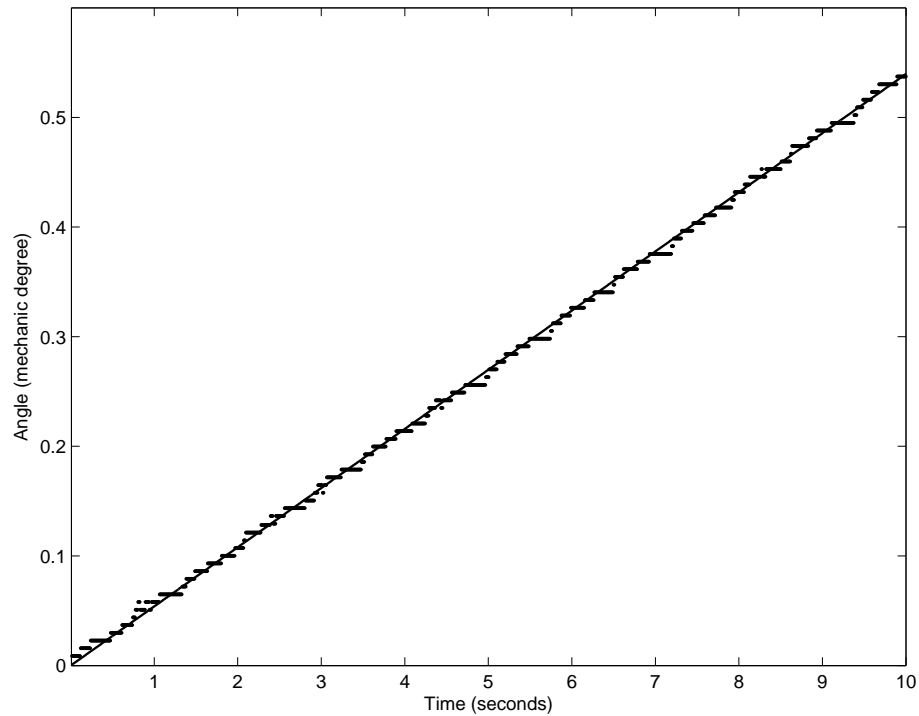


FIGURE 10.6: Open loop velocity control operating at $0.05^\circ/s$.

10.2.3 Step Response Angular Velocity

Comparing the steady state ripple in Figure 10.7 shows that increased rotational momentum reduces the impact of cogging torque. Overshoots in step response are due to the low pass filtering of the reference. This specific filter was originally intended for processing position references and as such there is room for improvement in designing a specific velocity reference filter which has no overshoot.

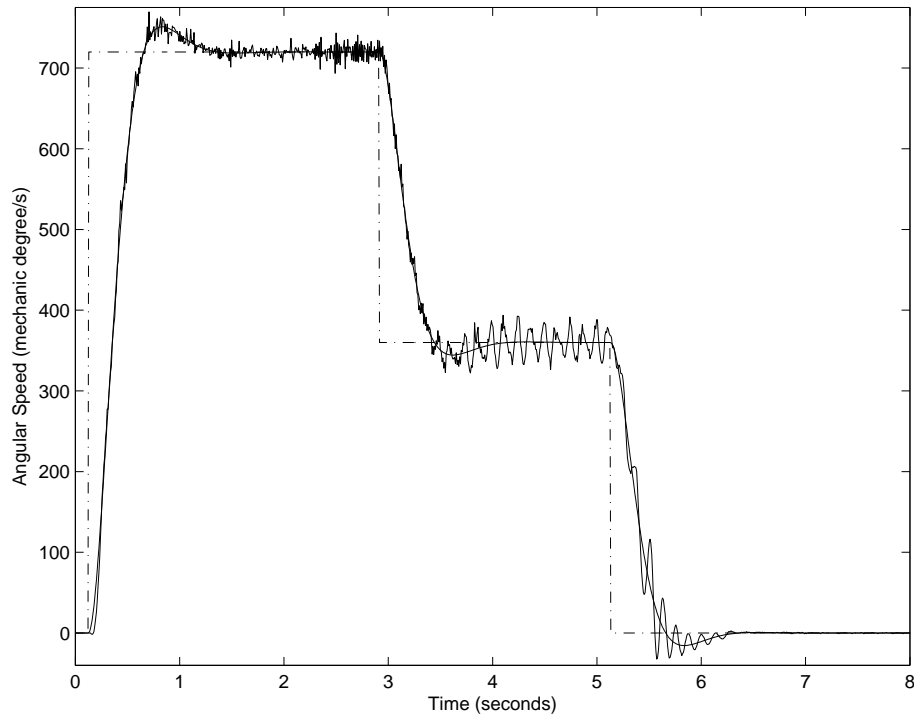


FIGURE 10.7: Angular velocity reference (dashed), filtered reference (line) and measured value (line).

Chapter 11

Compensation Methods

A number of compensation methods have been identified that could possibly improve performance of the field-oriented controller. All of them will be accounted for in this chapter. Those that were tested on the prototype will also be included in the result section at the end of this chapter.

11.1 Estimation of Speed

The straight forward method of Equation (5.3) is not always preferable. To use this estimate in applications a low pass filter needs to be applied to smoothen the measurements. However, a low pass filter introduces a phase lag which degrades performance in the controller. To overcome unwanted delay a Kalman Filter (KF) can be introduced. In the case with the PMSM the system transfer function Equation (6.17) is nonlinear. To apply KF to a nonlinear system linearization of the system can be done as in the Extended Kalman Filter (EKF) [31]. The EKF uses in most cases a first order linearization. There are second-order implementations but implementation and computational complexity make them hard to use [32]. The approximations made in the EKF can lead to non-optimal performance and the filter can also diverge [32][33]. To overcome the problems that arise from linearization in the EKF a method called the unscented Kalman filter (UKF) can be used [32][33]. The difference between EKF and UKF is in how the information is propagated. In the EKF the information is propagated through the linearized system and in the UKF the nonlinear system is used making it possible to capture nonlinear dynamics by the linearized system.

Compared to the KF, the UKF has a similar structure where a covariance and a gain matrix is predicted. The information is then used in a predictor/corrector scheme. In [34] UKF has been tested on a PMSM with some success.

Unfortunately Equation (5.4) implies that neither EKF nor UKF is helpful when operating at very low velocities. Accuracy of position measurement is considered to be very good and not using this measurement as input to the estimator can be considered as rash. The model also needs to include friction and cogging torque in order to approximate well at very low velocity. Taking these points into consideration it is doubtful that the EKF or UKF will improve velocity estimation.

11.2 Friction

When operating from zero to low velocities static friction creates an unwanted nonlinear behavior of the torque that needs to be applied to put the motor into motion and puts a high demand on bandwidth properties of the velocity controller. Compensation of friction can be done as in Figure 11.1. With the feedback of $\hat{P}_{friction}$ the nonlinearity can be reduced. Parameters of the friction can be estimated as a constant, with an observer [20] or adaptive control.

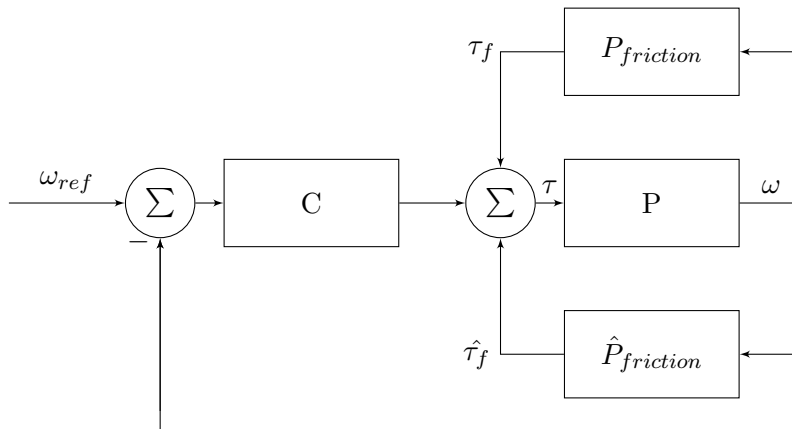


FIGURE 11.1: Closed loop system with process P modeled with friction separately as $P_{friction}$. Friction compensation is achieved through $\hat{P}_{friction}$.

The effects of cogging torque was dominating friction and it was of no use to evaluate friction compensation. If problem of cogging torque was solved then this compensation method would be of special interest.

11.3 Cogging Torque

11.3.1 Iterative Learning Control

In [35] an adaptive compensating controller in a form of angle based iterative learning control (ILC) has been proven to reduce the influence of cogging torque. The concept of the ILC is that the angular velocity error at a current rotor angle is filtered together with the angular velocity control output. This output will then be added as a compensation in the next revolution to reduce error introduced from the cogging torque, see Figure 11.2. An implementation of ILC described in [35] was tested. The output u of the next revolution is given by

$$u(i + 1, \theta_m) = Q(u(i, \theta_m) + Le(i, \theta_m)), \quad i = \text{iteration index} \quad (11.1)$$

where e is the control error, Q a low pass filter and L a transfer function.

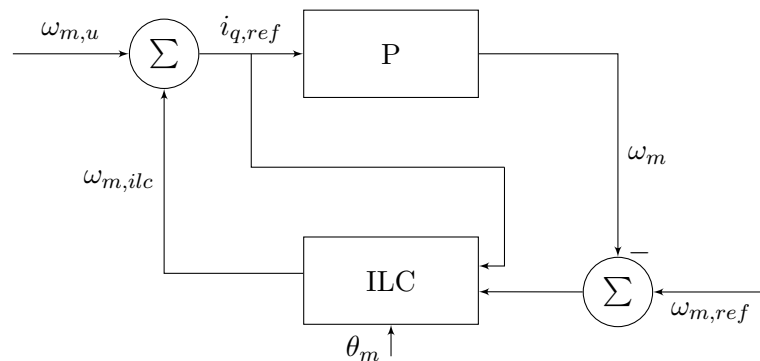


FIGURE 11.2: Block diagram of angle based ILC to reduce cogging torque. P includes both current feedback control and process.

11.3.2 Simulated Counter Torque

A heuristic approach is to simulate the cogging torque. The simulation result was implemented in a look-up table in the control solution. Dependent on rotor position this look-up table would inject a current that would, in theory, counteract the effect of the cogging torque at any given position. This solution demands that the estimated data would be precisely lined up with the actual cogging torque. For this reason cogging torque as a function of angular position was mapped in Section 11.3.3.

Simulation is done with *MotorSolve BLDC* from *Infolytica*. The software has a premade template for an outer rotor PMSM that is customizable in several ways. Naturally the accuracy of the simulation is dependent on the input data, most of which is unknown.

Educated guesses have been made whenever possible. 1280 data points have been gathered for a full electrical rotation, see Figure 11.3. This corresponds to the resolution of the sensor and storing any more values in the table is unnecessary. Having the data represented with fixed point and 16 bit resolution gives a total space requirement of 2.56 kB for the look-up table.

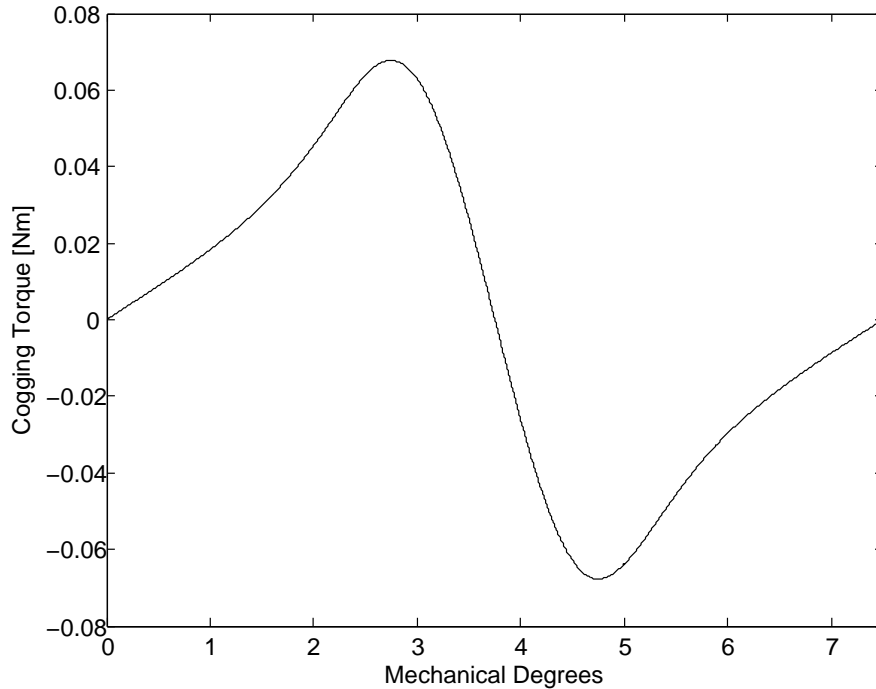


FIGURE 11.3: Output data from the finite element analysis. The period is 7.5 mechanical degrees indicating that this phenomenon occurs 48 times per revolution.

11.3.3 Angular Position Mapping

It is possible to visualize the nonlinear dynamics of the actual friction and cogging torque by moving the reference magnetic field and measure the torque angle, that is the relative error between the field and rotor position, see Figure 11.4. The main benefit of this measurement is to map rotor angle to cogging torque for use with detailed simulation. The resulting field vector is set so that it is barely strong and fast enough to continuously move the rotor. The error in torque is then estimated as

$$\tau = J_{rotor} \cdot \frac{\Delta^2 \delta}{(\Delta t)^2} \quad (11.2)$$

The very same magnetic field that makes it possible to move the rotor also introduces an error in the measurement that alternates between dampening and amplification of the perceived cogging torque depending on where the rotor is. Filtering of measurement data also contributes to the degradation of data reliability.

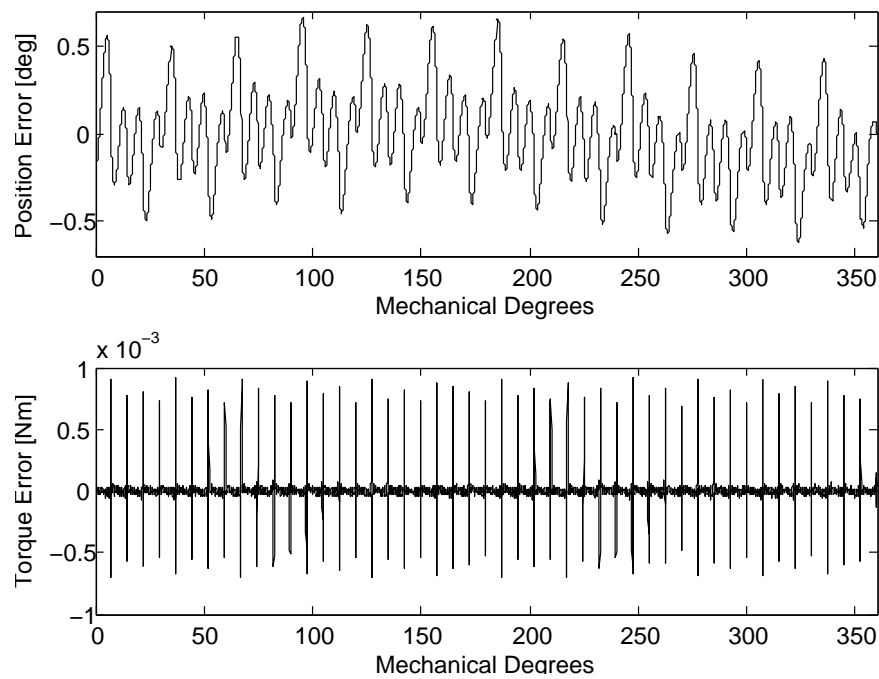


FIGURE 11.4: The mean value of position error is to be expected due to friction but a varying mean value across a rotation indicates some non-ideality in motor construction or that the sensor is nonlinear. The torque error plot is low pass filtered and the waveform has 48 periods per full revolution which corresponds to the simulation.

11.3.4 Sinusoidal Counter Torque

Assume that the actual and unknown cogging torque of the motor is described by Figure 11.3. Consider also that the position and frequency of cogging ripples for a full revolution is identified by measurements described in Figure 11.4. Then applying a counteracting sinusoidal waveform with correct frequency and phase in relation to the actual cogging torque gives the net torque in Figure 11.5. Since the maximum value of the actual cogging torque is unknown tuning should be done until ripple amplitude is minimized and its frequency has doubled. The scenario presented in this case gives a 47.7 % reduction of the cumulative absolute error.

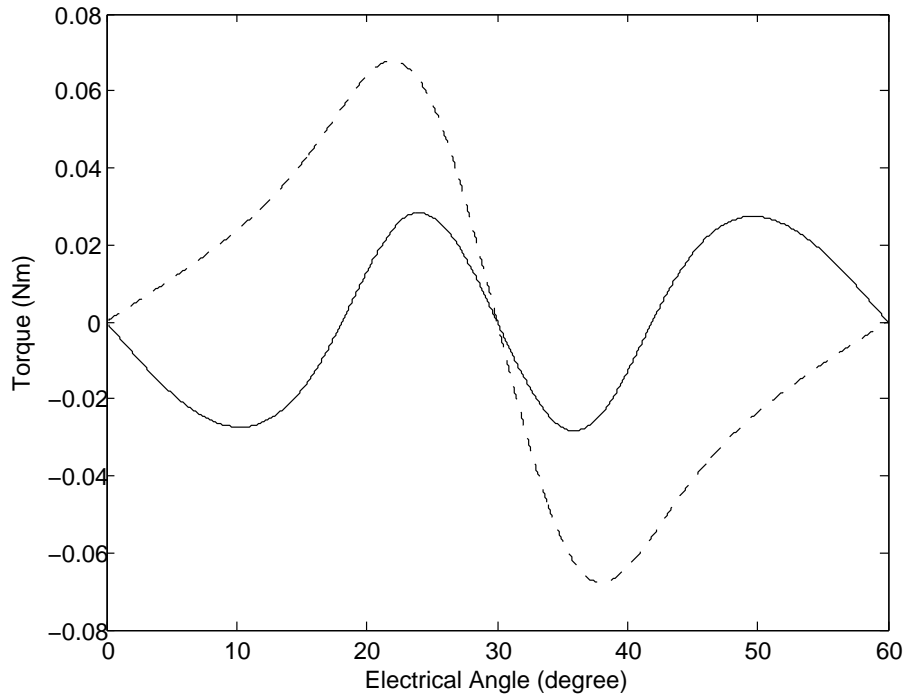


FIGURE 11.5: Imagined cogging torque (dashed) and difference torque (line).

11.4 Results

11.4.1 Iterative Learning Control

To allow the low angular velocity measurements sampling rate was set to 50 Hz not allowing the ILC to operate at a frequency where it was able to fully compensate for the highly dynamic cogging torque. However, some success was made with this method. A small angular velocity reference value of $10^\circ/s$ was given, leaving the ILC operating while the angular velocity controller was disabled. Successively the ILC completed a few revolutions before disabling the updating. In Figure 11.6 the output from the ILC after one revolution is shown. There is clearly a symmetry and a strong relation to the cogging torque. The difference is friction. Output from the ILC is generated from running in one direction only. The ILC will have to keep the output above the friction torque to enable motion. That is the reason for the offset from zero. The mean value is $\bar{i}_{q,ILC} = 0.0120mA$ which converted to torque is $\bar{\tau}_{ilc} = 0.116mNm \approx k_c$.

With this permanent ILC curve it was not possible to run as slow as $1^\circ/s$. Control was very oscillatory but a great improvement from $90^\circ/s$ that was achieved without compensation from ILC.

During tests with ILC it was noted that stability was not guaranteed for all values of L and Q [36]. Setting of these filters are critical for successful operation of the ILC. No further stability analysis was made.

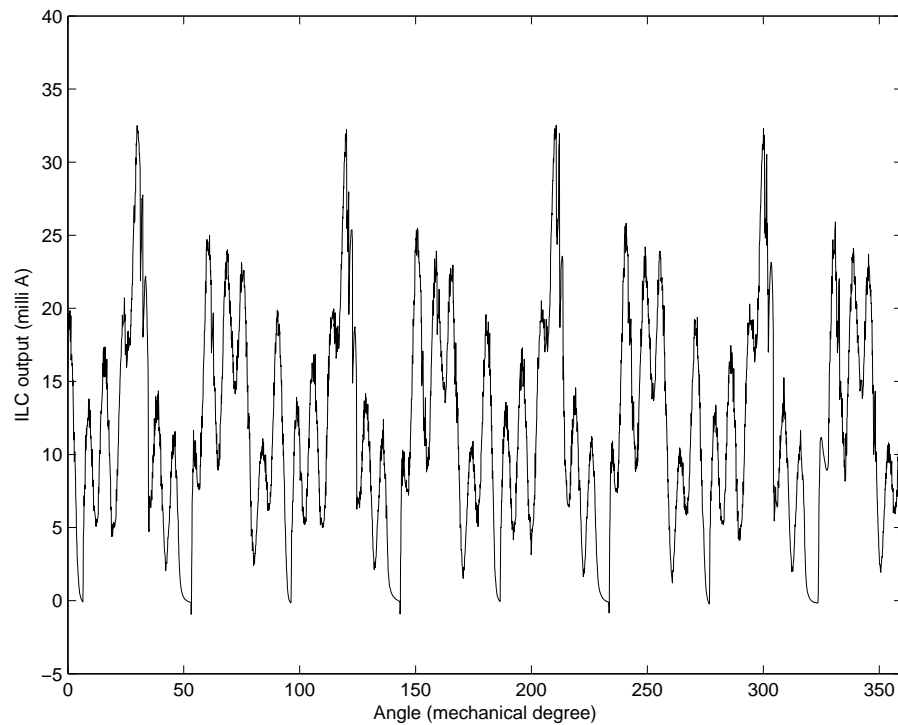


FIGURE 11.6: Output of ILC after one revolution.

In Figures 11.7, 11.8 and 11.9 a comparison between no compensation and compensation with ILC of a step response from 0-180° is shown. It is clear that angular velocity control has less transients in angular velocity and thus resulting in a step response for position which is much smoother but about 0.2 seconds slower.

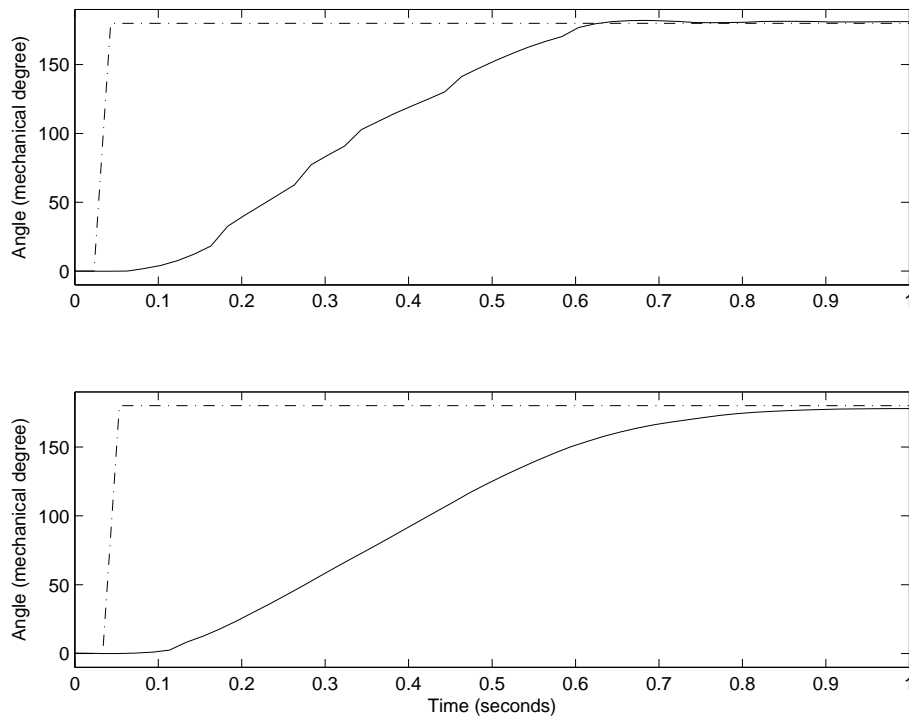


FIGURE 11.7: Position step response from 0 - 180° . Dashed line is reference value and solid line is measured value. The top plot is without compensation from ILC and the bottom plot with ILC enabled.

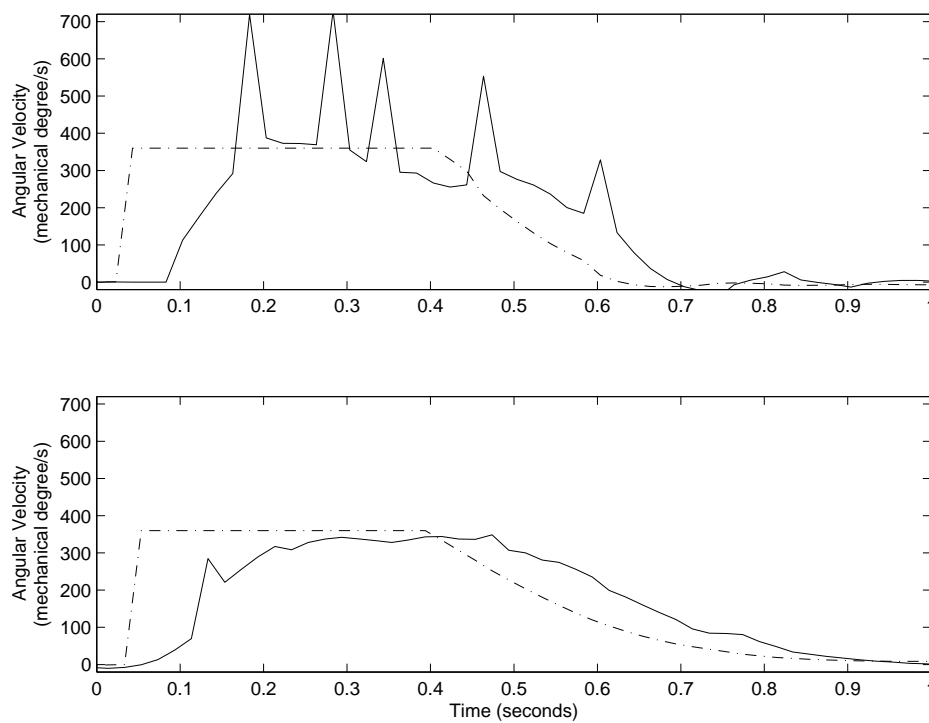


FIGURE 11.8: Angular velocity controller when acting on a position step response from 0 - 180° . Dashed line is reference value and solid line is measured value. The top plot is without compensation from ILC and the bottom plot with ILC enabled.

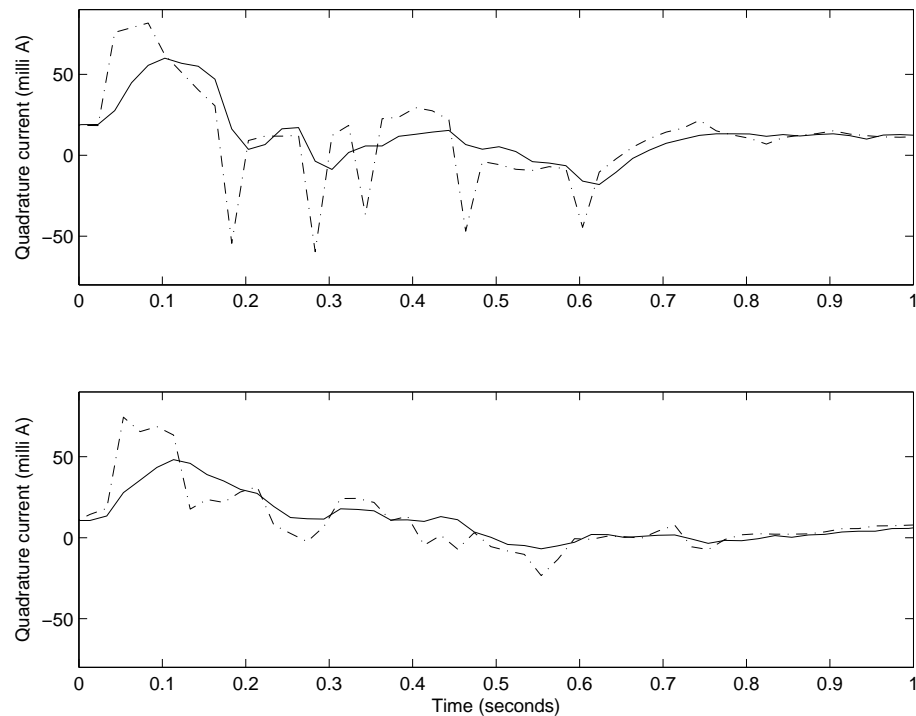


FIGURE 11.9: Current controller when acting on a position step response from 0-180°. Dashed line is reference value and solid line is measured value. The top plot is without compensation from ILC and the bottom plot with ILC enabled.

11.4.2 Simulated and Sinusoidal Counter Torque

The look-up tables based on these methods were tuned in phase and amplitude in relation to the cogging torque. However, the net effect of the compensation resulted in a somewhat smooth motion in parts of a mechanical rotation but a choppy motion in other parts. This behavior indicates most likely that the motor has uneven torque characteristics for a full mechanical rotation, as such this method was unsuccessful in solving the cogging torque problem.

Chapter 12

Discussion

One of the goals of this project was to derive a model of the PMM and then to investigate model parameters. The model is not an exact replication of the real world process, which of course is impossible. It does, however, mirror the behavior of the process to a high degree when comparing simulations with real world behavior. The process of identifying all the necessary model parameters has also been elaborated upon.

The work of determining a suitable control method ended up in two different solutions, each with its respective strengths and weaknesses. They are both equal in the fact that they are portable to a micro-controller.

FOC could not be successfully implemented for the application. Still simulations of the control law promises substantial improvements in rise time for position step responses. A greater understanding of what limits FOC in position applications has been gained by developing a detailed model of the process. From this model it is possible to evaluate the necessary sampling rate for the angular velocity controller, with or without cogging torque compensation. By determining the necessary sampling rate then hard requirements can be set on the position encoder resolution or gearing between rotor and encoder ring to increase the sampling rate. Without taking such requirements into account then future improvements on the prototype would be futile.

It remains uncertain whether or not the problems associated with this specific motor is common among other similar sized motors due to for example non-ideality introduced in production. However, if that is the case then attempts to nullify the cogging torque by simulation would prove ineffective. Actual torque measurements on the motor would most certainly be beneficial, but doing so in mass production would naturally increase production costs.

ILC would then seem to have the best of both worlds. It has potential to vastly improve low velocity performance of the FOC, while at the same time require no special consideration for characteristics of individual motors as the algorithm is adaptive. Therefore it can handle production variations of motors. The drawback is then that the motors need a number of low angular velocity rotations to tune its adaptive look up table. This could be done either during installation and setup of a camera or better yet during fabrication where the process could be automated. However, care has to be taken to verify stability of the algorithm or results can be disastrous.

The synchronous control method is slow although operationally stable in comparison to the FOC. It fulfills almost all the requirements set on the prototype. One should therefore carefully consider whether or not it is worth the hassle of overcoming the problems with the FOC. In addition to engineering hours for implementing the FOC it is also a more expensive method in manufacturing as it requires current sensing whereas the synchronous controller should be able to run current control in open loop.

The fact that the FOC can measure current is the main reason for its responsiveness. Current feedback enables it to maximize torque output per used ampere, making it highly efficient compared to the synchronous controller.

Chapter 13

Conclusion

The derived model for system simulation does replicate the fundamental behavior of the process. The motor driver designed for this project is functioning and serves as a platform for evaluating different control algorithms. The two control algorithms developed for the project are considered to be portable to MCU.

FOC is fast in step responses while being incapable of low speed operation as it requires faster sampling of velocity than is currently possible. The method does, however, show potential for improvement when ILC compensation is introduced.

The synchronous control method is slow although operationally stable in comparison to the FOC. Results were meeting almost all of the design criteria while leaving room for performance improvements regarding step response time and power consumption.

The performance of the two control methods are compared to the system requirements, see Table 13.1. The maximum and continuous power consumption requirements have been deliberately neglected as they were unable to be measured on the prototype.

TABLE 13.1: FOC and synchronous control performance compared to requirements

Description	FOC	Synchronous control
Minimum rotation velocity	Not fulfilled	Fulfilled
Time needed for half rotation	Almost fulfilled	Not fulfilled
Steady state position error without load	Not fulfilled	Fulfilled
Steady state position error with load	Not fulfilled	Fulfilled

The main contribution of this project is that it has shed light upon possibilities and limitations of two alternative control methods when applied to an unusual application.

13.1 Future Work

The following recommendations are made for future research for the FOC:

- Investigate solutions for measuring very low velocity while maintaining a high sample rate;
- Combine one or more cogging torque compensation methods with a higher resolution position encoder and determine stability conditions for the ILC.

As for synchronous controller research needs into the following subjects have been identified:

- Optimization of the offloading between quadrature current and torque angle for minimizing steady state power consumption;
- Determine performance impact of different types of reference filtering.

Bibliography

- [1] Axis Communications AB. Our business, 2014. URL http://www.axis.com/corporate/our_business/index.htm. Online; accessed 15-December-2014.
- [2] Axis Communications AB. Interim Report July-September 2014, 2014. URL <http://www.axis.com/documentation/corporate/reports/2014/q3powerpoint.pdf>. Online; accessed 15-December-2014.
- [3] M. Höst, B. Regnell, and P. Runeson. *Att genomföra examensarbete*. Studentlitteratur AB, Lund, 1:6 edition, 2006.
- [4] J.R. Hendershot. Brushless DC Motor Phase, Pole and Slot Configurations. *Magna Physics Corporation*, pages 1–8. URL http://www.jimhendershot.com/Jim_Hendershot/Articles_files/brushlessdcmotorphasepoleslotconfigurations.pdf. Online; Accessed 22-January-2015.
- [5] R. Krishna. *Permanent Magnet Synchronous and Brushless DC Motor Drives*. Taylor and Francis Group, LLC, 2010.
- [6] T. Reichert, T. Nussbaumer, and J.W. Kolar. Torque Scaling Laws for Interior and Exterior Rotor Permanent Magnet Machines. page 4, March 2009. URL https://www.pes.ee.ethz.ch/uploads/tx_ethpublications/Reichert_Transmag09_TorqueScaling_Final.pdf. Online; Accessed 22-January-2015.
- [7] C.M. Ta. Pseudo-vector control - An alternative approach for brushless DC motor drives. In *Electric Machines Drives Conference (IEMDC), 2011 IEEE International*, pages 1534–1539, May 2011. doi: 10.1109/IEMDC.2011.5994837.
- [8] National Instruments. crio-9022, . URL <http://www.ni.com/datasheet/pdf/en/ds-202>. Rev: 2014-11-06, Online; Accessed: 13-January-2015.
- [9] National Instruments. crio-916, . URL <http://www.ni.com/datasheet/pdf/en/ds-227>. Rev: 2014-11-06, Online; Accessed 13-January-2015.

- [10] National Instruments. 9215, . URL <http://www.ni.com/datasheet/pdf/en/ds-192>. Rev: 2014-11-06, Online; Accessed 13-January-2015.
- [11] National Instruments. 9401, . URL <http://www.ni.com/datasheet/pdf/en/ds-86>. Rev: 2014-11-06, Online; Accessed 13-January-2015.
- [12] Toshiba. M370 Group. URL <http://toshiba.semicon-storage.com/eu/product/microcomputer/lineup/arm-micon/tx03-series/m370-group.html>. Online; Accessed 2015-01-13.
- [13] Atmel. AVR32723: Sensor Field Oriented Control for Brushless DC motors with AT32UC3B0256 . *Atmel, Appl. Note*, Rev. 32126A-AVR32-06/09(AVR32723), 2009. URL <http://www.atmel.com/Images/doc32126.pdf>. Online; Accessed 14-January-2015.
- [14] Texas Instruments. DRV83x2 Three-Phase PWM Motor Driver, December 2014. URL <http://www.ti.com/lit/ds/symlink/drv8332.pdf>. Rev: SLES256E–May 2010–revised December 2014. Online; Accessed: 19-January-2015.
- [15] AMS AG. AS5311 High Resolution Magnetic Linear Encoder, 2013. URL http://ams.com/eng/content/download/17954/325059/file/AS5311_Datasheet_EN_v6.pdf. Rev. 1.12, Online; Accessed 19-January-2015.
- [16] Persson, E. and Takahashi, T. Eliminate Ripple Current Error from Motor Current Measurement. White paper, Advanced Development Group International Rectifier Corp. U.S.A. URL <http://www.irf.com/technical-info/whitepaper/motorcurrent.pdf>. Online; Accessed 14-January-2015.
- [17] LEM. Current Transducer LTSR 6-NP, February 2012. URL http://www.lem.com/hq/en/component/option,com_catalog/task,displaymodel/id,90.54.09.000.0/. Online; accessed 19-January-2015.
- [18] Maxon Motor AG. EC 45 flat, part number 251601, June 2014. URL http://www.maxonmotor.com/medias/sys_master/root/8813854326814/14-232-EN-Jun.pdf. Online; Accessed 19-January-2015.
- [19] Leadshine Technology Co., Ltd. Motor Torque Calculation. URL <http://www.leadshine.com/Pdf/Calculation.pdf>. Online; Accessed 19-January-2015.
- [20] C.C. De Wit, H. Olsson, K.J. Astrom, and P. Lischinsky. A new model for control of systems with friction. *Automatic Control, IEEE Transactions on*, 40(3):419–425, Mar 1995. ISSN 0018-9286. doi: 10.1109/9.376053.
- [21] S. Sánchez-Mazuca and R. Campa. An improvement proposal to the static friction model. *Mathematical Problems in Engineering*, pages 1 – 8, 2013. ISSN 1024123X.

- [22] Wikipedia. DQ0 transformation, 2015. URL http://en.wikipedia.org/wiki/Dqo_transformation#cite_note-Anderson-2. Online; Accessed 21-January-2015.
- [23] H. Hofmann and B. Hieb. Characterizing and validating a permanent magnet synchronous motor model. University of Michigan Lecture, 2012.
- [24] V. Bobek. PMSM Electrical Parameters Measurement. *Freescale Semiconductor, Inc., Appl. Note*, (AN4680):7–14, February 2013. URL http://cache.freescale.com/files/microcontrollers/doc/app_note/AN4680.pdf. Online; Accessed 19-January-2015.
- [25] Z. Li, S.Z. Jiang, and C.C. Chan. Comparison of alternate analytical models for predicting cogging torque in surface-mounted permanent magnet machines. In *Vehicle Power and Propulsion Conference, 2008. VPPC '08. IEEE*, pages 1–6, Sept 2008. doi: 10.1109/VPPC.2008.4677557.
- [26] N. Hemati and M.C. Leu. A complete model characterization of brushless dc motors. *Industry Applications, IEEE Transactions on*, 28(1):172–180, Jan 1992. ISSN 0093-9994.
- [27] H.W. van der Broeck, H. C. Skudelny, and G.V. Stanke. Analysis and realization of a pulsewidth modulator based on voltage space vectors. *Industry Applications, IEEE Transactions on*, 24(1):142–150, Jan 1988. ISSN 0093-9994. doi: 10.1109/28.87265.
- [28] D.O. Neascu. Space Vector Modulation - An Introduction, Tutorial at IECON2001. In *Industrial Electronics Society, 2001. IECON '01. The 27th Annual Conference of the IEEE*, pages 1583–1592, vol.1, 2001. URL <http://www.et.upt.ro/admin/tmpfile/fileM1224954797file490353adde0d4.pdf>. Online; Accessed 19-January-2015.
- [29] W.C. Duesterhoeft, M.W. Schulz, and E. Clarke. Determination of instantaneous currents and voltages by means of alpha, beta, and zero components. *American Institute of Electrical Engineers, Transactions of the*, 70(2):1248–1255, July 1951. ISSN 0096-3860.
- [30] S. de Pablo, A.B. Rey, L.C. Herrero, and J.M. Ruiz. A simpler and faster method for SVM implementation. In *Power Electronics and Applications, 2007 European Conference on*, pages 1–9, Sept 2007. doi: 10.1109/EPE.2007.4417751.
- [31] R. Johansson. *Predictive and Adaptive Control*. Lund University, Dept. Automatic Control, Sweden, 2008.

-
- [32] E.A. Wan and R. Van der Merwe. The unscented Kalman filter for nonlinear estimation. In *Adaptive Systems for Signal Processing, Communications, and Control Symposium 2000. AS-SPCC. The IEEE 2000*, pages 153–158, 2000. doi: 10.1109/ASSPCC.2000.882463.
- [33] S.J. Julier and J.K. Uhlmann. Unscented Filtering and Nonlinear Estimation. *Proceedings of the IEEE*, 92(3):401–422, March 2004. ISSN 0018-9219. doi: 10.1109/JPROC.2003.823141.
- [34] K. Zawirski, D. Janiszewski, and R. Muszynski. Unscented and extended Kalman filters study for sensorless control of PM synchronous motors with load torque estimation. *Bulletin of the Polish Academy of Sciences-Technical Sciences*, 61(4): 793 – 801, 2013. ISSN 02397528.
- [35] Y. Yuan, F. Auger, L. Loron, S. Moisy, and M. Hubert. Torque ripple reduction in permanent magnet synchronous machines using angle-based iterative learning control. In *IECON 2012 - 38th Annual Conference on IEEE Industrial Electronics Society*, pages 2518–2523, October 2012. doi: 10.1109/IECON.2012.6388853.
- [36] M. Norrlöf. Iterative Learning Control of Analysis, Design and Experiments. *Linköping Studies in Science and Technology*, (653), 2000. URL <http://users.isy.liu.se/en/rt/mino/pub/thesis653.pdf>.